


Generalist Vision-Language Models for Fast Radio Burst detection: a zero-shot benchmark against a specialized detector

Raiff H. Santos ^{*}, Amilcar R. Queiroz [†], K. E. L. de Farias [‡] and Rafael A. Batista [§]
*Universidade Federal de Campina Grande,
R. Aprício Veloso 882, Bairro Universitário,
58429-900, Campina Grande, PB, Brazil*

Tharcisyo S. S. Duarte [¶]
*Instituto de Formação de Educadores, Universidade Federal do Cariri,
Rua Olegário Emídio de Araújo, s/n, Aldeota, 63260-000, Brejo Santo, CE, Brazil and
Universidade Federal de Campina Grande,
R. Aprício Veloso 882, Bairro Universitário,
58429-900, Campina Grande, PB, Brazil*
(Dated: July 9, 2026)

Fast Radio Bursts (FRBs) are millisecond-duration radio transients whose automated detection increasingly relies on highly specialized deep learning models. These detectors achieve exceptional performance, but they require large task-specific training datasets and cannot be redefined without retraining. In this work, we evaluate whether small, open-weight, locally run generalist Vision-Language Models (VLMs) can detect FRBs in dynamic spectra under a zero-shot, prompt-only regime, with no fine-tuning and no labeled examples, returning structured decisions with a natural-language justification. From a controlled set of 3000 simulated L-band dynamic spectra containing FRBs, structured Radio Frequency Interference (RFI), and noise, we draw a balanced binary benchmark of 2000 samples and compare two such VLMs (Gemma 4 2B and 4B), sample by sample, against the state-of-the-art specialized detector SwinYNet. At the default threshold, Gemma 4 2B reaches an accuracy of 93.65%, with no statistically significant difference from SwinYNet (92.90%), while showing a significantly lower false-positive rate on structured RFI (6.4% vs. 25.0%) and no false positives on pure noise. SwinYNet retains a perfect probabilistic ranking on this benchmark (ROC-AUC of 1.0000 vs. 0.9482), a ceiling that the zero-shot VLM approaches from general-purpose pretraining alone. Rewriting the prompt alone reconfigures the same models for three-class FRB/RFI/noise classification on the full set of 3000 spectra, where they reach up to 86% accuracy without a single false FRB.

I. INTRODUCTION

Fast Radio Bursts (FRBs) are intense radio transients with durations of only a few milliseconds and predominantly of extragalactic origin. Since the discovery of the first FRB by [1], these events have become one of the most intriguing topics in modern astrophysics and cosmology [2–7]. FRBs are characterized by their large dispersion measures (DMs) [3, 8, 9], which generally exceed the expected contribution from the Milky Way, indicating propagation through the ionized intergalactic medium (IGM). Over the past years, hundreds of FRBs have been detected by several radio observatories, including the Parkes telescope, CHIME [10], ASKAP [11], FAST [12], and MeerKAT [13], revealing a diverse population of repeating and apparently non-repeating sources. Because of their extragalactic characteristics, they have recently been used for cosmological probes in several scenarios [14–20].

Processing these streams in real-time requires automated detection pipelines. Traditional pipelines rely on matched filtering and dedispersion, which are computationally expensive [6, 21–23]. Historically, this process was dominated by CPU-based software packages like PRESTO (PulsaR Exploration and Search TOolkit) [24, 25], which established the foundational algorithms for incoherent dedispersion [26] and candidate folding [27]. To cope with the escalating data rates of modern radio telescopes, the field transitioned toward GPU-accelerated architectures, such as the Heimdall pipeline [26], which enabled high-throughput single-pulse searches in real-time. More recently, the paradigm has shifted toward mitigating the computational burden of brute-force dedispersion altogether by introducing visual and morphological feature extraction [28]. A key example is RaSPDAM (Radio Single-Pulse Detection Algorithm Based on Visual Morphological Features) [29], an AI-driven framework that treats the dynamic spectrum as a computer vision problem to rapidly identify transient candidates. Extending this visual approach to its current state-of-the-art, advanced Vision Transformer (ViT) architectures [30] have established a powerful new paradigm for end-to-end processing. Specifically, models like SwinYNet [31] represent a major shift in FRB search by performing multi-task learning that simultaneously combines real-

* raiffhugos@gmail.com

† amilcarq@df.ufcg.edu.br

‡ klecio.lima@uaf.ufcg.edu.br

§ rafael.batista@uaf.ufcg.edu.br

¶ tharcisyo.duarte@ufca.edu.br

time burst detection, pixel-level signal segmentation, and direct parameter estimation from raw dynamic spectra without any prior dedispersion. While these specialized deep learning models achieve exceptional performance, they traditionally rely on large, specialized astronomical datasets for training. As an alternative to training such dedicated models from scratch, the rapid advancement of Multimodal Large Language Models (MLLMs) [32], or Vision-Language Models (VLMs), has introduced a parallel paradigm where generalist foundation models can be applied directly to visual classification tasks using only natural language prompts.

This paradigm has already begun to be explored in astronomical problems, including galaxy morphology classification [33, 34] and domain-adapted astronomical assistants [35, 36]. In optical transients, it was shown in Ref. [37] that a generalist Large Language Model (LLM), Google’s Gemini [38], can approach the performance of a convolutional neural network in classifying real sources versus artifacts (*real versus bogus*) across three surveys (Pan-STARRS, MeerLICHT, and ATLAS) with the advantage of generating human-readable descriptions for each candidate from a few examples and concise instructions. That same work, however, points to an important practical limitation. Employing a large LLM through a commercial API is, at present, infeasible at the scale of upcoming surveys (such as the Vera Rubin Observatory, which is expected to generate on the order of 10 million alerts per night), both because of token-generation latency and prohibitive costs. The authors indicate as promising directions the fine-tuning of smaller open-source LLMs, with one to two billion parameters, and model quantization to enable faster local inference. It is precisely in this direction that models such as Gemma 4 have advanced, providing open, small, locally executable VLMs [39], the central premise of the approach we adopt here.

Applications to radio data have also begun to appear, although still relying on fine-tuning and outside the domain of FRBs. In Ref. [40], STARWHISPER-PULSAR was proposed, which fine-tunes an MLLM over visual, textual, and numerical modalities to distinguish pulsar candidates from noise, outperforming specialized machine-learning methods. In Ref. [41], the RadioAstroVQA set was built and MLLMs were fine-tuned for image classification and visual question answering (VQA) in radio astronomy, achieving accuracy comparable to or higher than that of existing deep-learning models. Similarly, in Ref. [42], a VLM, radio-llava, was fine-tuned for the analysis and classification of radio-astronomical sources. On the other hand, in Ref. [43], the authors evaluated generalist VLMs (Qwen and Gemini) on the morphological classification of radio galaxies (MiraBest FR-I/FR-II). Prompt-only strategies already achieve good performance, but the outputs are unstable, varying strongly with superficial changes to the prompt, while a light fine-tuning (LoRA) rivals specialized models. Taken together, these works confirm the potential

of MLLMs and VLMs in astronomy, but they typically resort to fine-tuning, to large models accessed through an API, or to tasks distinct from FRB detection.

In this paper, in contrast, we present a systematic evaluation of small, local VLMs (Gemma 4 2B and 4B) applied to the task of FRB detection. We construct a controlled, simulated benchmark of 3000 L-band dynamic spectra, from which we draw a balanced binary subset of 2000 samples, using `simulateSearch` [44] containing FRB signals, various classes of structured Radio Frequency Interference (RFI), and background noise. We compare the zero-shot, prompt-only performance of these VLMs against SwinYNet, a state-of-the-art specialized deep learning detector. We analyze their performance across binary and multiclass tasks, evaluate their behavior as probabilistic classifiers, characterize their failure modes on faint signals, and discuss the computational trade-offs of deploying generalist models in operational astronomical pipelines.

This paper is structured as follows. Section II reviews the physics of Fast Radio Bursts and their dispersive signature, the RFI and noise that contaminate the search, and the traditional single-pulse pipelines used to detect them. Section III introduces multimodal models and the class of VLMs evaluated in this work. Section IV details the simulation setup and benchmark dataset. Section V describes the zero-shot VLM classification protocol and prompt design. Section VI presents the quantitative results, paired comparison with SwinYNet, and error analyses. Finally, Section VII summarizes our findings and outlines directions for future work.

II. FAST RADIO BURSTS, RFI, AND TRADITIONAL SEARCHES

This section provides the physical and operational background for the classification task studied in this work. The goal is not a complete review of FRB astrophysics or of transient-search software, but a concise account of three points on which the rest of the paper depends: what an FRB looks like in a dynamic spectrum, what the two contaminants a search must reject, viz. RFI and noise, look like in the same representation, and how a traditional pipeline turns a raw data stream into candidates. The detection task is fundamentally binary: an FRB must be separated from everything that is not an FRB, whether structured interference or background noise. This is the decision that both the specialized detector and the generalist VLM perform in our comparison. The VLM, however, is not restricted to this binary decision. It can also be prompted to go beyond it and separate RFI from noise as well, a possibility we return to later in Sect. V G.

A. The dispersed burst and its visual signature

A Fast Radio Burst is a radio transient of millisecond duration, high energy, and predominantly extragalactic origin [1], although a bright radio burst from the Galactic magnetar SGR 1935+2154 has tied at least some FRBs to magnetars [45]. As the broadband pulse propagates through the ionized plasma of the interstellar and intergalactic media, its lower frequencies are progressively delayed relative to the higher ones, an effect known as dispersion [27]. The resulting delay between two frequencies ν_{lo} and ν_{hi} is set by the DM through

$$\Delta t = \frac{e^2}{2\pi m_e c} (\nu_{\text{lo}}^{-2} - \nu_{\text{hi}}^{-2}) \text{DM}, \quad (1)$$

and

$$\text{DM} = \int_0^d n_e(l) dl, \quad (2)$$

where $n_e(l)$ is the free-electron density along the path. The observed DM combines contributions from the Milky Way, the intergalactic medium, and the host galaxy [46]:

$$\text{DM}_{\text{obs}}(z) = \text{DM}_{\text{MW}} + \text{DM}_{\text{IGM}} + \frac{\text{DM}_{\text{host}}}{1+z}. \quad (3)$$

A DM in excess of the expected Galactic contribution [47, 48] is one of the primary indicators of an extragalactic source. Other propagation effects (scattering, scintillation, Faraday rotation, and plasma lensing, among others) further modify the pulse, but dispersion is the effect that dominates its appearance and underlies its detection.

Because the delay scales as ν^{-2} , an FRB traces a characteristic curved track in the dynamic spectrum, the time–frequency plane in which the horizontal axis is time, the vertical axis is frequency, and the pixel intensity is signal power. Lower frequencies arrive systematically later, so the burst appears as a single, localized, plausibly broadband sweep whose curvature is set by the DM. This quadratic sweep is the visual signature a search must recover, and it is exactly the morphology the VLM is asked to identify from the image alone (Sect. V). Dispersion is also what most cleanly separates an astrophysical burst from terrestrial interference, since the latter does not, in general, follow the same frequency-dependent delay [49].

B. Radio-frequency interference and noise

The negative class of an FRB search is dominated by two very different phenomena: RFI and system noise. RFI is contamination of terrestrial or instrumental origin like, for instance, mobile networks, wireless links, radar, satellites, power lines, and the receiver electronics themselves. Because these sources sit far closer to the telescope than any astrophysical emitter, RFI is frequently

orders of magnitude stronger than the signal of interest and can bury a genuine burst [49].

Crucially, RFI is not a single visual class. It appears as persistent narrowband bands (nearly horizontal lines at fixed frequencies), as broadband impulses with no dispersive delay (nearly vertical, zero-DM structures), as periodic or repetitive patterns, and as multiband or in-band occupancy from services such as wireless networks and satellites. What these morphologies share is the absence of the coherent ν^{-2} sweep of a dispersed burst. This makes them dangerous since some of them can partially imitate coherent structure and then survive as false candidates. System noise, by contrast, is the stochastic fluctuation of the instrument, with no coherent structure. It matters because dispersion spreads the burst energy over a wide time span and lowers its signal-to-noise ratio, letting faint bursts sink into the background. These two contaminants map directly onto the RFI and NOISE classes of our benchmark (Sect. IV), whose distinct behavior is what motivates reporting false positives separately for each (Sect. VID).

C. Traditional single-pulse searches

Because the DM of a candidate is not known in advance, a traditional single-pulse search cannot look for the sweep directly; it must reconstruct the burst by testing many trial DMs [29, 49]. After the strongest interference is flagged and masked in time and frequency, the search proceeds by dedispersion. For a given trial DM, each frequency channel is shifted back in time by the delay that this DM predicts, and the channels are summed into a single time series. When the trial DM matches the burst, the curved sweep re-aligns and the burst energy piles up into one narrow, high signal-to-noise (S/N) spike; when it does not, the channels add out of step and the energy smears back into the background. The two-dimensional search for a curved track is thereby reduced to a one-dimensional search for a peak, repeated over a dense grid of trial DMs. A genuine burst reaches its maximum S/N at its true DM and falls off on either side, whereas terrestrial interference, having no dispersive delay, peaks at zero DM; the trial DM that maximizes the response therefore both estimates the dispersion and helps distinguish the burst from RFI.

Each dedispersed time series must still be searched for a pulse of unknown duration. This is done by matched filtering. The series is correlated with boxcar templates of increasing width, and the S/N is largest when the template width matches the true burst width, since a narrower window discards signal while a wider one adds noise. Samples exceeding an S/N threshold, over the joint space of trial DM, arrival time, and boxcar width, are retained as single-pulse candidates. Because a real event produces detections at many neighboring trials, these are then clustered to collapse each event into a single candidate, which is finally labeled as astrophysical or as a

false positive (historically by human inspection, and increasingly by machine-learning classifiers). This scheme underlies the standard search tools, from the CPU-based PRESTO [24, 25] to the GPU-accelerated Heimdall [26], and it remains the dominant approach to FRB detection.

The cost of this procedure is dominated by dedispersion. Direct incoherent dedispersion scales as $O(N_t N_\nu N_{\text{DM}})$ in the number of time samples N_t , frequency channels N_ν , and trial DMs N_{DM} ; with hundreds to thousands of DM trials at high time and frequency resolution, a brute-force real-time search becomes very expensive [26]. This burden has driven both the move to GPU acceleration and, more recently, a shift toward treating the dynamic spectrum as an image and applying computer-vision models to it directly, as in RaSP-DAM [29], DRAFTS [49], and SwinYNet [31].

D. Limitations of the traditional approach

Beyond raw computational cost, the traditional pipeline has well-known operational limitations. The DM grid is redundant, so a single event is detected at many trial DMs and inflates the candidate list with duplicates. The output is dominated by false positives, most of them driven by RFI that survives the masking stage or is even introduced by it [49]. Performance is highly sensitive to parameter choices, like the RFI-flagging algorithm, the spacing of the DM grid, the set of boxcar widths, and the S/N threshold, so that faint bursts near the detection limit are easily lost. And because the surviving candidates must still be separated from residual interference, the pipeline ultimately relies on human verification, which becomes the practical bottleneck as data volumes grow [31].

These limitations frame the rest of the paper. The RFI-driven false-positive rate and the human-inspection bottleneck are exactly the pressure points that learning-based methods try to relieve, and the fact that the FRB signature is, at bottom, a visual pattern in the dynamic spectrum is what makes an image-level approach natural. It is against this backdrop that we ask a narrower question: how much of that recognition is already within reach of a generalist VLM applied to the dynamic-spectrum image, with no domain-specific training at all.

III. MULTIMODAL MODELS AND VLMS

This section characterizes the model class evaluated in this work and the operational regime adopted. The goal is not an exhaustive review of multimodal machine learning, but a concise account of how a generalist VLM, with no FRB-specific training, can be applied to dynamic-spectrum images, and how its performance should be interpreted as a lower bound on the potential of the approach.

A. From language models to Vision-Language Models

MLLMs extend LLMs to non-textual inputs [32]. An LLM represents text as a sequence of *tokens*, discrete units (typically subwords) that the model reads and generates. VLMs are the subclass that jointly conditions on an image \mathbf{I} and a textual instruction \mathbf{p} to produce a textual response \mathbf{y} . In the dominant connector architecture [50], a vision encoder \mathcal{E}_v maps the image to visual tokens, a projector W_v aligns them with the LLM embedding space, and an autoregressive decoder generates the answer:

$$\mathbf{z} = W_v \mathcal{E}_v(\mathbf{I}), \quad p(\mathbf{y} | \mathbf{I}, \mathbf{p}) = \prod_{t=1}^T p(y_t | y_{<t}, \mathbf{z}, \mathbf{p}). \quad (4)$$

Here, \mathbf{z} are the visual tokens already projected into the embedding space, and the response is generated token by token in an autoregressive way. Each token y_t is produced conditioned on the previous tokens $y_{<t}$, the visual tokens \mathbf{z} , and the prompt \mathbf{p} , over the T tokens of the response. Because the output is free text, the same structure can perform captioning, visual question answering, or, as in this work, systematic classification, depending solely on the prompt.

This generality, that is, a single model serving distinct tasks according to the instruction, comes from the pretraining regime. These models are trained on large collections of general-domain text and image-text pairs, which gives them broad visual and linguistic knowledge but does not specialize them in any particular scientific task. Throughout the paper, following the introduction, we use *VLM* for this class of models applied to dynamic-spectrum images. The extent to which this general competence transfers to specialized scientific imagery is an open question, now actively probed by dedicated multimodal benchmarks in astronomy [51–53].

B. Zero-shot classification and the prompt-only regime

In this work, the VLMs operate in a zero-shot, prompt-only regime. *Zero-shot* means that the model classifies each spectrum without having been exposed to any labeled example of the task, relying solely on the representations acquired during general multimodal pretraining and on a textual instruction that specifies the candidate classes. This use of natural language to reference visual concepts learned in pretraining, rather than a classifier head fitted to task-specific labels, is precisely the transfer mechanism introduced by CLIP [54], here applied to dynamic spectra. *Prompt-only* means that no model weight is updated. The task is defined entirely in natural language.

This regime is therefore distinct from *in-context* (few-shot) learning, in which a handful of labeled examples

would be embedded in the prompt as demonstrations, a strategy adopted, for instance, in the classification of optical transients with LLMs [37] and of radio galaxies with VLMs [43].

It is equally distinct from the other common strategies for adapting foundation models. There is no fine-tuning, i.e., no weight adjustment on FRB data; no retrieval-augmented generation (RAG), in which external documents would be injected into the prompt; and no agentic behavior or external tool calls. The model receives a single image and a single instruction, and returns a decision. This choice is deliberate, as it isolates the question of interest: how much of the ability to recognize an FRB is already latent in a generalist model, prior to any domain specialization? Accordingly, the performance reported here should be interpreted as a measure of potential, not as the ceiling the approach would reach with further adaptation.

C. Generalist and specialized detectors

The central difference between a generalist VLM and a detector such as SwinYNet lies in the origin of its competence. SwinYNet is a supervised model built on the Swin Transformer backbone [55], trained end to end on FRB data to jointly perform detection, segmentation, and parameter estimation, and it operates on the PSRFITS files in its native domain. Formally, both approaches can be written as a composition of a visual feature extractor f_θ and a task head g_ϕ ,

$$\hat{y} = g_\phi(f_\theta(x)), \quad (5)$$

but they differ in how the parameters (θ, ϕ) are obtained. In the specialized detector, both θ and ϕ are optimized on labeled FRB data,

$$(\theta^*, \phi^*) = \arg \min_{\theta, \phi} \mathcal{L}_{\text{FRB}}. \quad (6)$$

In the zero-shot VLM, θ is fixed from general multimodal pretraining and the task head is induced by the textual prompt P rather than fitted, so that $\hat{y} = g_P(f_\theta(x))$ with θ unchanged.

Applying the VLM to FRB detection is therefore a test of visual transfer: checking whether a feature map f_θ learned in a general domain, encoding edges, elongated tracks, textures, and localized structures, is already expressive enough to separate a dispersed burst from interference and from noise, without any update to θ . This is the same hierarchical, multiscale feature reuse that makes the Swin backbone an effective general-purpose vision model [55], here probed in the opposite regime, reused as-is, instead of fine-tuned.

This asymmetry is part of the study design and is examined in detail in the methodological comparison

(Sect. VH). It favors the specialized detector in terms of access to information, which is precisely what makes strong VLM performance interesting. The argument of the paper is not that the VLM replaces a dedicated detector, but that a generalist tool already recognizes the relevant patterns starting from almost no domain information, supporting the potential thesis.

D. Small, local, and open models

A deliberate aspect of the study is the use of small, open-weight models that run locally, rather than large models accessed through a commercial API or the large, domain-specific foundation models now being trained for astronomy [56]. This choice is enabled by a recent generation of compact open models, such as the Gemma family [57], which are explicitly designed to be deployable across hardware ranging from consumer devices to servers, bringing state-of-the-art capability within reach of modest infrastructure.

The motivations are practical. Local execution removes the dependence on commercial services and per-call costs; it favors reproducibility, since a specific model version can be pinned and rerun; it keeps the data under the control of whoever performs the analysis; and it makes the approach accessible to groups without large computational infrastructure. Small models also bring the experiment closer to a realistic deployment scenario in radio astronomy, where candidate screening may need to happen near the instrument and under hardware constraints.

The cost of this choice is a per-model capability lower than that of the largest available systems. We argue that this works in favor of the analysis rather than against it. The performance reported here is therefore a *conservative floor* for what the class of generalist VLMs could reach, since a larger model operating in the same prompt-only regime would be expected to match or exceed it. The two concrete models evaluated, their versions, and the hardware used are described in Sect. VB.

E. Structured output and interpretability

Because they produce text, VLMs can be instructed to respond in a structured format and, at the same time, to justify the decision in natural language. In this work, the model returns a label, a continuous probability that the image contains an FRB, a confidence, and a short justification accompanied by visual attributes, with the exact schema shown in Listing 1. This property is attractive for scientific use, because each decision comes with an inspectable explanation, something that specialized detectors rarely offer.

Even so, this justification should be treated as auditable auxiliary data, not as automatic physical proof.

A model can produce a plausible explanation for an incorrect decision. Therefore, interpretability here is understood as inspectability of the decision, not as a guarantee of physical causality, a point taken up again among the threats to validity (Sect. VIH).

IV. SIMULATION AND DATASET

This section describes the experimental design used to build the set of dynamic spectra evaluated in this work. The goal is not to reproduce the full complexity surrounding real observations. The idea is to create a controlled, balanced, and reproducible benchmark to compare generalist VLMs with a specialized detector on the same samples. For this reason, the instrumental configuration was chosen to approximate the conditions used in the evaluation of SwinYNet, making the comparison more informative without presenting the set as a real observational validation. An overview of the complete pipeline, from simulation to the paired comparison of results, is shown in Fig. 1.

A. Motivation for using simulated data

The use of synthetic data is a deliberate methodological choice in this first experiment. In real observational data, labels can be ambiguous, incomplete, or dependent on later decisions of human inspection. In a study that seeks to measure whether a generalist VLM recognizes visual patterns associated with FRBs, RFI, and noise, this ambiguity would make it difficult to separate model error from uncertainty in the label itself.

With simulation, each sample has a known ground truth. For the FRB examples, the physical parameters of the injected event are recorded in the metadata, including arrival time, DM, width, flux density, reference frequency, and profile type. For the RFI examples, the interference category and the parameters used in the generation are also preserved. For noise, the sample is defined as the absence of an injected coherent structure, containing only system noise.

Simulation also makes it possible to control the statistical composition of the benchmark. The benchmark for the binary task was built in a balanced way, containing the same number of `FRB` and `NON_FRB` samples. This prevents the initial metrics from being dominated by an arbitrary class prevalence and makes the comparison between the VLM and the specialized detector more direct. The real prevalence of FRBs in astronomical surveys is much lower, but the goal of this stage is to evaluate the discriminative capability in a controlled environment.

Another important advantage is reproducibility. The pipeline uses a global seed and per-sample derived seeds. The same set can therefore be regenerated by other researchers as long as they use the same configuration, the same code version, and an equivalent environment for

simulateSearch. This property is especially relevant because the article compares models sample by sample, not only by aggregate metrics.

B. Generation of the PSRFITS files

The data were generated with simulateSearch [44, 58], a package for simulating high time-resolution radio observations. The software allows one to compose system noise, dispersed transient signals, and different forms of RFI, producing files in search-mode PSRFITS format [59]. These files can be processed by conventional astronomical tools and, in this work, also serve as the source for the dynamic-spectrum images supplied to the VLMs.

Each simulated file corresponds to 2 s of observation. The configuration used has 2048 frequency channels, a time sampling of 1.96608×10^{-4} s, and 8-bit quantization. In practice, each sample contains approximately 10 173 time samples. The system noise level was varied reproducibly per sample through a dimensionless scale applied to the 25 K base T_{sys} , yielding an effective system temperature between 16.25 K and 36.25 K and preventing the global noise level from being a fixed class cue.

Table I summarizes the main instrumental parameters used in the generation.

C. Benchmark composition

The simulation produced a full set of 3000 samples, with 1000 examples of each source class (`FRB`, `RFI`, and `NOISE`). The benchmark used in the binary evaluation is a balanced subset of 2000 of these samples, summarized in Table II. The positive class is composed of the 1000 `FRB` examples. The negative class `NON_FRB` contains 1000 examples, split equally between 500 `RFI` examples and 500 `NOISE` examples. The remaining 500 `RFI` and 500 `NOISE` samples are not discarded; the full set of 3000 is used in the multiclass task (Sect. VI G). The original labels are preserved in the metadata to allow diagnostic analyses, but the main task of the article aggregates `RFI` and `NOISE` into `NON_FRB`, since this is the most direct formulation for comparison with a binary FRB detector.

This separation between the binary label and the source class is important for interpreting the results. Two samples incorrectly classified as `FRB` may have very different physical or instrumental causes. One may be rare stochastic noise, while another may be structured `RFI`. Preserving the source class makes it possible to estimate false-positive rates separately for `RFI` and noise, which became one of the central analyses of the article.

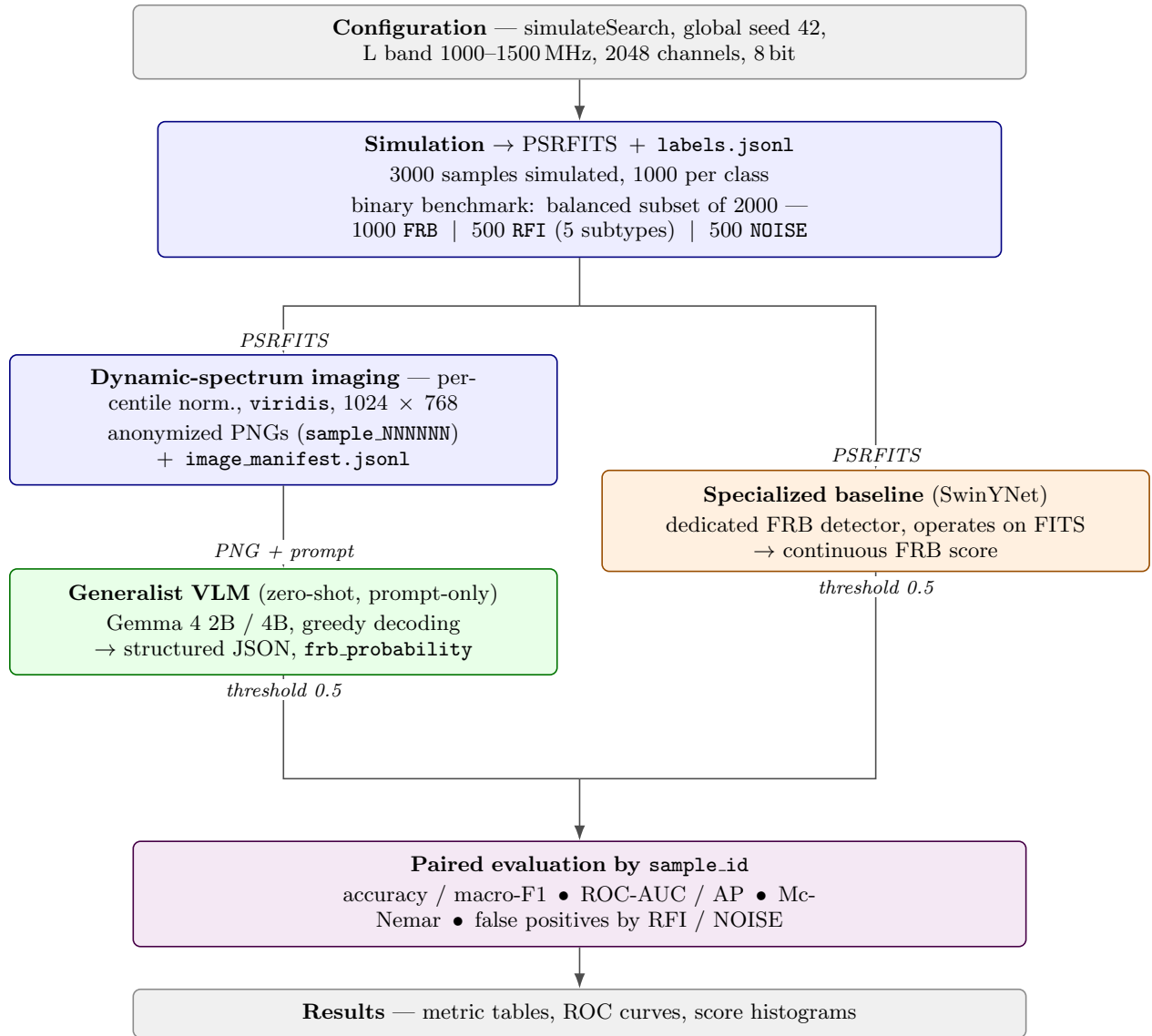


FIG. 1. Overview of the end-to-end pipeline, from simulation to results. A controlled set of 3000 dynamic spectra (1000 per source class) is simulated with simulateSearch, producing native PSRFITS files; the binary benchmark shown here is a balanced subset of 2000 samples (1000 FRB, 500 RFI across five subtypes, and 500 NOISE). These PSRFITS then feed two independent detectors through different paths. For the generalist VLM (Gemma 4 2B/4B) they are first rendered as anonymized PNG images, which the model classifies from the image and a fixed prompt alone, whereas the specialized baseline SwinYNet operates directly on the native PSRFITS. Each produces a continuous FRB score thresholded at 0.5, and the two are then compared sample by sample through the shared `sample.id`. The deliberate input asymmetry, a rendered image for the VLM versus the native FITS for SwinYNet, is part of the experimental design.

D. Parameters of the simulated FRBs

For the FRB class, each sample receives a dispersed burst with reproducibly drawn parameters. In the metadata of the current set, the DM ranges from approximately 120.70 to 899.14 pc cm^{-3} , the temporal width ranges from 0.003 to 0.005 s, and the flux density ranges from approximately 4.02 to 11.98 in the internal units used by the simulation. The arrival time, the reference frequency, the dispersion index, and the profile type also

vary.

These variations are relevant because they prevent the VLM from memorizing a single FRB morphology. Instead, the model must recognize a family of visual patterns associated with dispersed transients, such as temporal localization, broadband structure, and a systematic delay with frequency. Since the study does not estimate the DM directly, it enters here as a generation parameter and as a diagnostic variable for future work, not as a prediction target in this first article.

TABLE I. Main instrumental parameters used in the generation of the simulated files.

Parameter	Value
Instrumental reference	aligned to SwinYNet domain
Start frequency	1000 MHz
End frequency	1500 MHz
Number of channels	2048
Time sampling	1.96608×10^{-4} s
Duration per file	2 s
Time samples per file	≈ 10173
Quantization	8 bits
Gain	0.7
Base system temperature	25 K
T_{sys} scale per sample (dimensionless)	0.650187 to 1.449952
Effective system temperature	16.25 K to 36.25 K
Maximum FRB width	0.005 s
Global seed	42

TABLE II. Composition and class mapping of the binary benchmark dataset. The 2000 total samples are evenly distributed between the target class (FRB) and the negative class (NON_FRB), which combines structured interference (RFI) and background NOISE.

Source class	Binary label	Number of samples
FRB	FRB	1000
RFI	NON_FRB	500
NOISE	NON_FRB	500
Total		2000

TABLE III. Distribution of the 500 RFI samples of the binary benchmark across distinct interference categories. The benchmark includes five balanced categories (100 samples each) representing common environmental and anthropogenic interference types, ranging from continuous narrow-band signals to transient broad-band events.

RFI category	Number of samples
persistent_narrowband	100
impulsive_broadband	100
wifi_multiband	100
point_to_point_microwave	100
satellite_like_inband	100

E. RFI and noise

The RFI examples were simulated to represent structured interference capable of confusing an automatic transient search. The full simulated set contains five categories, balanced with 200 samples each, of which 100 per category enter the binary benchmark (Table III).

These categories cover both persistent contamination in frequency and impulsive or multiband events. This diversity is important because RFI is not a single visual class. Some samples may appear as persistent horizontal lines, others as broadband impulses, multiband structures, or patterns that occupy specific regions of the

band. A useful classifier must separate these morphologies from a dispersed track compatible with an FRB.

The NOISE examples, in turn, represent samples without an injected coherent structure. They are important to test whether the model confuses random fluctuations with FRB candidates. The reproducible variation in the system noise level is applied to all classes, including FRB, RFI, and NOISE, to reduce the risk that the classifier uses only the global brightness or the mean contrast as a decision cue.

F. Conversion to dynamic-spectrum images

After the PSRFITS were generated, each file was converted into a PNG dynamic-spectrum image. In these images, the horizontal axis represents time, the vertical axis represents frequency, and the pixel intensity represents signal power. This representation was chosen because it corresponds to the type of visual input that a VLM can process directly. One representative example of each class is shown in Fig. 2.

In the experimental run described here, the images were generated with percentile normalization, in which the pixel intensities are linearly scaled between the 1st and 99th percentiles of each dynamic spectrum and clipped to this range, with the `viridis` colormap, a width of 1024 pixels, and a height of 768 pixels. These parameters were recorded in the image manifest to keep the evaluation auditable. The choice of normalization and colormap can influence the performance of visual models; for this reason, it must be treated as part of the experimental protocol, not as a purely aesthetic detail.

The VLM receives only the final image and the textual classification instruction. It does not receive the FITS file, the simulation parameters, the DM, the true label, or any numerical metadata. This choice creates an important difference relative to SwinYNet, which operates on FITS files and can exploit a specialized pipeline. The comparison is therefore deliberately asymmetric. The

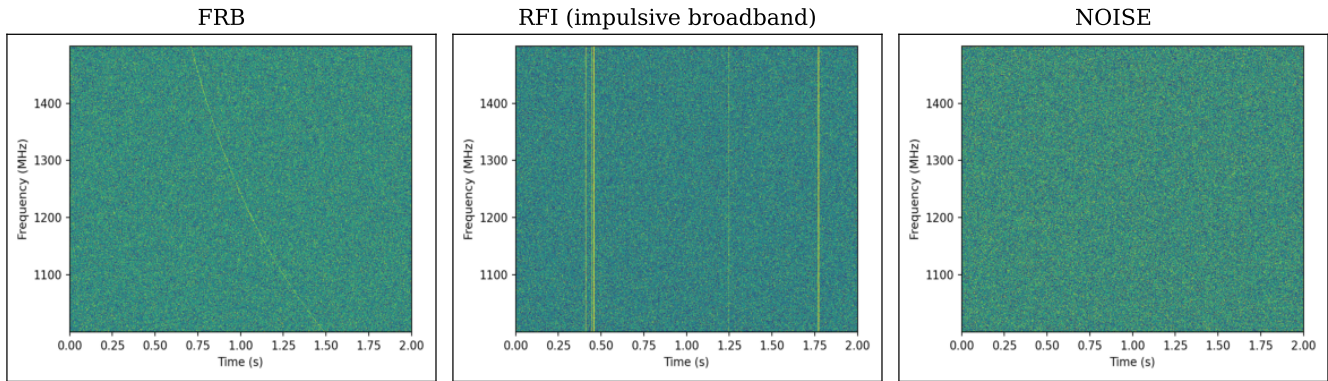


FIG. 2. Representative anonymized dynamic-spectrum images, one per class, as supplied to the VLM. Left: an FRB (a single dispersed broadband transient); middle: RFI of the `impulsive_broadband` type (broadband impulses localized in time); right: NOISE (system noise only). In each panel the horizontal axis is time, the vertical axis is frequency, and the pixel intensity is signal power (viridis colormap, percentile normalization).

specialized detector receives an input closer to its natural domain, while the VLM operates on a single visual representation.

G. Anonymization and leakage control

A central methodological point is to prevent label leakage. If the file name, the directory, or the image title contained terms such as FRB, RFI, or NOISE, a VLM could exploit that textual cue instead of analyzing the dynamic spectrum. To avoid this, the images supplied to the model were saved in a neutral directory, with anonymous names in the format `sample_000000.png`, `sample_000001.png`, and so on.

The image manifest preserves the link between the anonymous identifier, the source FITS, the simulation parameters, and the true label. This manifest is used only by the evaluation pipeline. The anonymous image path is the only path needed for VLM inference, and the images have no title with class information. In this way, the prediction must depend on the visual content of the dynamic spectrum.

This leakage control is also important for external comparison. The files and manifests make it possible to align predictions by `sample_id` without exposing the source class to the classifier. The aggregate metrics and the paired comparison can thus be computed later without contaminating the classification stage.

H. Reproducibility and generated artifacts

The pipeline design explicitly separates data, images, predictions, and metrics. The simulation generates the PSRFITS files and the label metadata; the plotting stage generates the anonymized images and the visual manifest; the classification produces per-sample predic-

tions; and the evaluation computes aggregate metrics and paired analyses. This separation makes it possible to repeat a single stage, audit inputs and outputs, and compare different models on exactly the same samples.

The main artifacts used in this stage are:

- `dataset/fits/`: simulated PSRFITS files;
- `dataset/images/samples/`: anonymized images supplied to the VLM;
- `dataset/metadata/labels.jsonl`: labels and simulation parameters;
- `dataset/metadata/image_manifest.jsonl`: link between the anonymous image, the source FITS, and the true label.

This set of artifacts defines the benchmark used in the following sections. From it, Sect. V describes how the images were presented to the VLMs, how the responses were structured, and how the predictions were aligned with the outputs of the specialized detector.

V. USING A VLM FOR FRB DETECTION

This section describes how the VLMs were used to classify the images generated in Sect. IV. The central point of the protocol is that the models were not trained, fine-tuned, or specialized for radio astronomy. They receive only the anonymous dynamic-spectrum image and a fixed textual instruction. The experiment thus tests a specific question. To what extent can a generalist VLM, used in a prompt-only regime, recognize visual patterns associated with FRBs and separate them from RFI and noise?

The main task of the article is binary, FRB versus NON_FRB, to allow a direct comparison with the specialized detector. The multiclass formulation, FRB/RFI/NOISE, reveals a natural advantage of VLMs

and reinforces the potential thesis, by showing that the task can be redefined through the prompt without changing the model weights.

A. Input supplied to the model

Each sample sent to the VLM consists of an anonymous PNG dynamic-spectrum image. The image is accompanied by a textual instruction, but no simulation metadata is provided to the model. In particular, the VLM does not receive the true label, the original FITS file name, the source class, the DM, the RFI parameters, or any identifier containing FRB, RFI, or NOISE.

The instruction informs only how to interpret the image visually, with the horizontal axis as time, the vertical axis as frequency, and the pixel intensity as signal power. The model must infer the class from the visual morphology of the dynamic spectrum. This restriction is important because it differentiates the VLM task from the task of the specialized detector. The VLM operates on a single image, while SwinYNet is evaluated in its natural domain, from FITS files and its own processing pipeline.

B. Models evaluated

Two models from the Gemma 4 family were evaluated (Table IV). The smaller variant is referred to throughout the article as Gemma 4 2B, and the larger variant as Gemma 4 4B. Both are generalist, open-weight multimodal models that can be run locally. In the protocol of this work, they are used strictly in zero-shot mode, that is, no weight is updated, no FRB-specific training set is used, and no labeled example is included in the prompt as a demonstration.

This choice is deliberate. A specialized supervised classifier, such as SwinYNet, is expected to be a strong reference because it was designed for FRB searches. The VLM, on the other hand, is tested as a generalist model. Therefore, the result of interest is not only the final metric, but the capacity for visual transfer. Can the model apply general visual and textual knowledge to a specialized scientific domain without fine-tuning?

Local execution is also part of the motivation. Small models reduce the dependence on commercial APIs, per-token costs, and remote infrastructure. However, the operational evaluation must be made with caution. In the measured run, Gemma 4 2B took on average 5.4 s per file and Gemma 4 4B took 7.8 s per file, while each simulated file contains 2 s of observation. These values indicate feasibility for candidate triage or hybrid pipelines, but they do not, by themselves, demonstrate a brute-force real-time search.

The timing measurements above were obtained on a workstation with an Intel Xeon w9-3495X processor (56 cores / 112 threads, up to 4.8 GHz), about 1 TB of

RAM, and 4 NVIDIA RTX 4500 Ada Generation GPUs (24 GB each). Inference was run with the Hugging Face Transformers library [60], using `device_map="auto"`, the model’s native precision, and greedy decoding, processing one image at a time, without batching. It is worth noting that the models themselves are small enough to fit on a single 24 GB GPU and were designed for execution on consumer hardware: Gemma 4 2B targets mobile devices and Gemma 4 4B targets personal computers.¹ The reported times therefore reflect this specific configuration, in a sample-by-sample regime and without optimization, and should be read as indicative, not as the latency expected on a typical phone or personal computer.

C. Binary prompt and structured output

In the binary task, the prompt asks the model to classify each image as `FRB` or `NON_FRB`. The instruction defines `FRB` as a single localized transient, plausibly broadband, with a frequency-dependent arrival trend. The prompt also makes explicit that cases dominated by random noise, persistent bands, repetitive patterns, broadband impulses without a dispersion delay, saturation, blank regions, or normalization artifacts must be classified as `NON_FRB`. The full binary prompt used is reproduced in Appendix A.

The expected response is a JSON object. The most important field for the evaluation is `frb_probability`, a continuous estimate of the probability that the image contains an FRB. In addition, the model returns a textual label, a confidence in the discrete label, a short justification, and boolean visual attributes. The expected structure is shown in Listing 1.

It is worth clarifying how `frb_probability` is obtained, since it does not come from a closed-form formula computed over the image pixels. The value is reported by the model itself in the corresponding JSON field, in response to the prompt instruction to estimate, in the interval $[0,1]$, the probability that the image contains an FRB. The prompt provides a calibration guide that associates probability ranges with different degrees of visual evidence, from a clear, textbook broadband dispersed sweep (0.95–0.99) to an unambiguous artifact such as saturation or clipping (0.01–0.04), and is reproduced in full in Appendix A. The pipeline only validates and lightly normalizes this number, converting any percentages to the $[0,1]$ scale and clamping to the valid interval, and then uses it directly as the continuous score in the ROC and Precision-Recall curves; the binary label comes from the same score through the 0.5 threshold, as described in Sect. V D. Because it is a number that the model chooses, and not a quantity derived from the internal token probabilities, in practice `frb_probability` takes few distinct values, a quantization discussed in Sect. VIB.

¹ <https://ai.google.dev/gemma/docs/core>

TABLE IV. Vision-Language Models evaluated and their role in the study.

Model	Role in the study	Usage mode	Mean time per file
Gemma 4 2B	Smaller generalist VLM	zero-shot, prompt-only	5.4 s
Gemma 4 4B	Larger generalist VLM	zero-shot, prompt-only	7.8 s

Listing 1. Expected JSON structure returned by the model in the binary task.

```

{
  "label": "FRB|NON_FRB",
  "frb_probability": 0.0,
  "confidence": 0.0,
  "reason": "short explanation referencing the visual evidence",
  "features": {
    "visible_structure": true,
    "broadband": true,
    "localized_transient": true,
    "frequency_dependent_delay": true,
    "persistent_bands": false,
    "repeating_pattern": false,
    "uniform_or_constant_background": false,
    "saturated_or_clipped": false,
    "random_background_texture": false
  }
}

```

Separating `frb_probability` from `confidence` avoids a common ambiguity in evaluations with LLMs. The FRB probability represents the continuous score used for ROC curves, Precision-Recall curves, and calibration analysis. The confidence, on the other hand, represents only the degree of certainty declared by the model about the discrete label. For this reason, the probabilistic analyses of the article use `frb_probability`, not the `confidence` field.

D. Binary decision and operating threshold

The binary label used in the metrics is derived from `frb_probability` by a decision threshold. The default threshold is 0.5. Samples with `frb_probability` ≥ 0.5 are evaluated as FRB, and samples below this value are evaluated as NON_FRB. This procedure ensures that the discrete decision is consistent with the continuous score used in the performance curves.

The textual label produced by the model is preserved, but it is not the primary source of the decision when a valid probability exists. If the model's text and the probability diverge, the sample receives a content warning for auditing, instead of being re-run until it produces a more convenient response. This methodological decision avoids rejection sampling and makes the evaluation more honest.

E. Deterministic decoding

All VLM inferences were made with deterministic decoding, in greedy mode, without sampling. In practice, this corresponds to the use of temperature 0. Parameters such as `top_p` and `top_k` are not activated in this regime. The goal is to reduce the stochastic variation between runs, since the same image, the same prompt, and the same model should produce the same response, within the limitations of the execution environment. This choice responds, in part, to the instability observed in generalist VLMs, whose outputs can vary with factors such as the decoding temperature [43]. By fixing deterministic decoding, we eliminate this stochastic component of the variation, although not the sensitivity to the prompt design itself, taken up again in Sect. VIH.

This choice is important for reproducibility. If sampling were used, part of the differences between models or runs could reflect decoding variation, not visual capability. Since the study compares the VLMs with a specialized detector in a paired evaluation, reducing this source of variance makes the interpretation of the disagreements clearer.

F. Handling invalid responses and execution failures

The protocol separates execution failures from content failures. Transient errors, such as input/output problems, timeouts, or recoverable memory failures, may allow retries. Invalid content responses, such as malformed JSON or the absence of `frb_probability`, are not re-

sampled. The raw response is preserved, the sample is flagged with a warning, and the evaluation records the occurrence.

This distinction is essential in order not to inflate performance artificially. If the model could be called repeatedly until it produced a valid and coherent JSON, the evaluation would also measure a response-selection strategy, not just the model’s first decision. In the results reported for the binary task, all 2000 samples were evaluated with no samples discarded due to error or invalid response.

G. Multiclass task by prompt

Besides the main binary task, the same pipeline allows a multiclass formulation with the three labels `FRB`, `RFI`, and `NOISE`. In this mode, the prompt defines the dispersed burst and pure stochastic noise explicitly, and treats `RFI` as a residual class that collects any coherent structure that is neither of the two. The multiclass task is not used as the main axis of comparison with SwinYNet, because the specialized baseline is analyzed here in the binary formulation. Even so, the multiclass task is indeed relevant.

The interest of the multiclass task is to show that the role of the VLM can go beyond an `FRB` versus `NON_FRB` decision. On receiving a different instruction, the model can attempt to separate false positives associated with `RFI` from samples dominated by pure noise. This flexibility is an important property of generalist models, since the task can be redefined through natural language, without retraining and without changing the architecture.

In this work, this flexibility is treated as supporting evidence of the potential of the VLMs, not as the central axis of the evaluation. The main quantitative comparison remains the paired binary analysis against SwinYNet, and the multiclass task does not compete with it; it adds a demonstration that the same tool, without retraining, still distinguishes `FRB`, `RFI`, and `NOISE` when the prompt asks for three classes.

H. Comparison with the specialized detector

The VLM predictions are compared with the SwinYNet predictions by anonymous sample identifier. The comparison is paired: each `sample_id` has a true label, a VLM prediction, and a prediction from the specialized detector. This alignment makes it possible to measure not only aggregate metrics, but also agreements and disagreements sample by sample.

The specialized baseline was used exactly as released by its authors, with no retraining, fine-tuning, or architectural modification. We ran SwinYNet version 1.0.0,

obtained from the official repository,² with the pre-trained weights distributed by the authors and the inference configuration provided in the released implementation. Inference was applied to anonymized copies of the simulated PSRFITS files, carrying the same neutral `sample_NNNNNN` identifiers used for the images, so that the leakage control described in Sect. IV also holds for the specialized detector. Each detection reported by the model carries a confidence value, which is taken as its continuous FRB score.

For the binary comparison, the external SwinYNet outputs are normalized to the same representation used by the evaluation pipeline, with a continuous FRB score and a binary decision at the 0.5 threshold. When an external model produces more than one detection for the same sample, the maximum score across the detections is used as the sample-level probability before the metrics are computed.

It is important to stress again the input asymmetry between the approaches. SwinYNet operates on the FITS files and was developed specifically for FRB searches, including steps that can exploit physical and temporal information in more detail. The VLM receives only an anonymous PNG of the dynamic spectrum and a textual instruction. The comparison should therefore not be interpreted as a direct competition between equivalent architectures, but as a measure of the potential of a generalist approach against a reference specialized detector.

In the following results section, this paired structure is the basis to answer three questions: which model has the best aggregate performance at the default threshold?; how do the models behave as probabilistic classifiers?; and in which types of `NON_FRB`, especially `RFI` or noise, each approach tends to produce false positives?

I. Evaluation metrics

To answer these three questions, the predictions of the two VLMs and of SwinYNet are evaluated on exactly the same 2000 samples, taking `FRB` as the positive class. The metrics used throughout the paper are defined below and apply to all the tables in the following sections, grouped into three sets: threshold-dependent metrics, probabilistic (threshold-independent) metrics, and statistical tests for the paired comparison.

Threshold-dependent metrics. Once the decision threshold is fixed, each binary prediction is a true positive (TP), a false positive (FP), a false negative (FN), or a true negative (TN). From these counts, the accuracy is the fraction of correctly classified samples,

$$\text{accuracy} = \frac{\text{TP} + \text{TN}}{\text{TP} + \text{TN} + \text{FP} + \text{FN}}. \quad (7)$$

² <https://github.com/expnn/SwinYNet>

The precision of a class is the fraction of correct predictions among the samples predicted in that class, and the recall is the fraction of the samples of that class that the model recovered,

$$P = \frac{TP}{TP + FP}, \quad R = \frac{TP}{TP + FN}. \quad (8)$$

The F1 score is the harmonic mean of precision and recall, and the macro-F1 is the unweighted mean of the per-class F1 scores,

$$F_1 = \frac{2PR}{P + R}. \quad (9)$$

The false-positive rate (FPR) is the fraction of negative samples classified as positive,

$$\text{FPR} = \frac{FP}{FP + TN}, \quad (10)$$

also reported separately for RFI (FPR_{RFI}) and for noise ($\text{FPR}_{\text{NOISE}}$), using only the samples of each type.

Probabilistic metrics. Independent of the threshold, these metrics evaluate the continuous `frb_probability` score directly. The ROC-AUC is the area under the ROC curve and equals the probability that the model assigns a higher score to an FRB than to a `NON_FRB` drawn at random, so that 1.0 indicates a perfect ranking and 0.5 indicates no discrimination. The Average Precision (AP) summarizes the Precision-Recall curve through the precision averaged over the recall gains. The Brier score [61] is the mean squared error between the predicted probability and the true label, and the ECE (Expected Calibration Error) [62] measures the mean deviation between the predicted confidence and the observed accuracy; for both, lower values indicate better calibration.

Paired-comparison tests. To compare two models on the same samples, the McNemar test [63] checks whether the disagreements between them are statistically significant, with low p-values indicating a real difference at the considered threshold, and the bootstrap confidence intervals [64] quantify the uncertainty of the differences (deltas) in ROC-AUC and AP between the models. Finally, in the multiclass task, the support of a class is the number of true samples of that class in the evaluated set.

VI. RESULTS AND DISCUSSION

This section gathers the quantitative results of the binary FRB versus `NON_FRB` task. The comparison involves three systems evaluated on exactly the same 2000 balanced samples, namely the two generalist VLMs Gemma 4 2B and Gemma 4 4B, used only with a prompt, and the specialized detector SwinYNet, taken as a performance reference. The set contains 1000 FRB and 1000 `NON_FRB`, with the negative class split into 500 RFI and 500 NOISE, and all samples were evaluated by the three models, with

no record discarded due to inference error or invalid response.

The discussion follows the three questions raised at the end of Sect. VH. The aggregate performance at the default threshold is addressed in Sect. VIA, the behavior of the models as probabilistic classifiers in Sects. VIB and VIC, and the origin of the false positives in each type of `NON_FRB` in Sect. VID. Results and discussion appear together because the main metrics require immediate interpretation.

A. Binary performance at the default threshold

Table V summarizes the discrete metrics at the default operating threshold of 0.5. The central result of this section is that both generalist VLMs, without any task-specific training and operating only with a prompt, achieve strong performance, with accuracy between 0.90 and 0.94 in separating FRB from `NON_FRB`. At the 0.5 operating point, Gemma 4 2B recorded an accuracy of 0.9365 and a macro-F1 of 0.9364, values close to those of the specialized supervised detector SwinYNet (accuracy 0.9290, macro-F1 0.9286); Gemma 4 4B obtained an accuracy of 0.9045 and a macro-F1 of 0.9039. As Sect. VIB makes clear, this proximity at the 0.5 threshold should not be read as superiority of the VLM over SwinYNet; the specialized detector has a perfect probabilistic ranking on this benchmark. It shows that a generalist model can reach performance similar to that of a dedicated detector starting from almost no domain information.

The most important reading of the table is not a simple ranking of the models, but the error profile of each approach. SwinYNet recovered all the FRBs at the default threshold (FRB recall of 1.0000), that is, it produced no false negatives for the positive class. In contrast, it classified 142 `NON_FRB` samples as FRB, reducing the precision of the positive class to 0.8757. Gemma 4 2B was less complete for FRB (recall of 0.9050), but rejected the negative class better (`NON_FRB` recall of 0.9680). Gemma 4 4B was even more conservative, with higher precision for FRB (0.9821), but lower FRB recall (0.8240).

This contrast of profiles is informative. SwinYNet behaves as a detector oriented toward high recall, minimizing FRB losses. The VLMs, especially Gemma 4 2B, operate more selectively at the 0.5 threshold, rejecting the negative class better. Therefore, a generalist model that displays this selective behavior without specific training is already an indication of the potential of the approach, taken up again in Sect. VID. The confusion matrices in Table VI reinforce this interpretation.

In the table, TP represents correctly identified FRBs, FN represents missed FRBs, FP represents `NON_FRB` samples classified as FRB, and TN represents `NON_FRB` samples correctly rejected.

A point that deserves explicit comment is that the larger VLM performs worse than the smaller one at this operating point (accuracy 0.9045 against 0.9365).

TABLE V. Discrete metrics at the default operating threshold of 0.5, for the three systems, with precision and recall reported separately for `FRB` and for `NON_FRB`. The metrics are defined in Sect. VI.

Model	Accuracy	Macro-F1	Precision (FRB)	Recall (FRB)	Precision (NON_FRB)	Recall (NON_FRB)
Gemma 4 2B	0.9365	0.9364	0.9658	0.9050	0.9106	0.9680
Gemma 4 4B	0.9045	0.9039	0.9821	0.8240	0.8484	0.9850
SwinYNet	0.9290	0.9286	0.8757	1.0000	1.0000	0.8580

TABLE VI. Confusion matrices at the 0.5 threshold, with `FRB` as the positive class. TP, FN, FP, and TN are defined in Sect. VI.

Model	TP	FN	FP	TN
Gemma 4 2B	905	95	32	968
Gemma 4 4B	824	176	15	985
SwinYNet	1000	0	142	858

The score distributions discussed in Sect. VI B indicate the origin of this inversion. Gemma 4 4B assigns low `frb_probability` values more often than Gemma 4 2B (1161 against 1063 of the 2000 samples fall below the 0.5 threshold), so the fixed cut converts more faint FRBs into false negatives (176 against 95), even though the larger model rejects RFI slightly better (Sect. VI D). The inversion therefore reflects a more conservative scoring profile interacting with the fixed threshold and with the coarse quantization of the self-reported score, rather than a generalized visual deficit of the larger model; in the multi-class task of Sect. VI G, Gemma 4 4B is consistently the better of the two.

B. Probabilistic performance

The continuous metrics, reported in Table VII, place the performance of the VLMs relative to the ceiling of the specialized detector. SwinYNet showed perfect probabilistic discrimination on this benchmark, with a ROC-AUC of 1.0000 and an Average Precision of 1.0000; that is, in the imported data, every `FRB` sample received a score above the highest `NON_FRB` score (the lowest `FRB` score, 0.999999, exceeds the highest `NON_FRB` score, 0.999864), which separates the classes perfectly by ranking. The generalist VLMs fall below this ceiling, but close to it: Gemma 4 2B obtained a ROC-AUC of 0.9482 and an AP of 0.9336, and Gemma 4 4B obtained a ROC-AUC of 0.9309 and an AP of 0.9102, a strong probabilistic performance for models without specific training. The corresponding ROC curves are shown in Fig. 3.

This contrast requires a careful reading, so as neither to exaggerate nor to underestimate the result. Since SwinYNet ranks the classes perfectly, at an optimal threshold it would classify without errors; the 142 false positives it shows in Sect. VI A are an effect of the fixed 0.5 threshold, not a limit of the model. Hence, the accuracy proximity between Gemma 4 2B and SwinYNet

at the 0.5 point is, in part, a threshold artifact, and not evidence that the VLM is superior. The defensible conclusion is the opposite, and more interesting for the thesis of this article. Even starting from a perfect ceiling of the dedicated detector, a zero-shot generalist VLM recovers most of this discriminative capability (ROC-AUC in the 0.93–0.95 range) without seeing a single labeled example.

It is also necessary to interpret these continuous metrics with caution, because of a limitation present in the results. The probabilities emitted by the VLMs are strongly quantized (Fig. 4). Gemma 4 2B used only three values of `frb_probability` across the entire benchmark — 0.15 (996 samples), 0.25 (67), and 0.85 (937) — and Gemma 4 4B used nine distinct values. In practice, `frb_probability` currently functions more as an ordinal confidence level than as a continuous score, so that ROC-AUC, AP, ECE, and the Brier score derive from curves with very few operating points. SwinYNet, on the other hand, saturates at or extremely close to 1.0 for the positive samples. For this reason, these numbers should be read as a diagnostic of the scoring behavior in this implementation, not as a definitive probabilistic calibration of the models.

C. Paired comparison with SwinYNet

The sample-by-sample comparison, summarized in Table VIII, makes it possible to assess whether the differences at the 0.5 threshold are statistically evident and whether the models err on the same cases. Gemma 4 2B and SwinYNet agreed on 1793 of the 2000 samples and disagreed on 207. Among the disagreements, Gemma 4 2B was correct in 111 cases in which SwinYNet erred, while SwinYNet was correct in 96 cases in which Gemma 4 2B erred. The McNemar test produced $p = 0.3305$, so the discrete difference between the two models at this operating point is not statistically significant under the approximation used.

Gemma 4 4B showed a different profile. It disagreed with SwinYNet on 307 samples. It was correct in 129 cases in which SwinYNet erred, but SwinYNet was correct in 178 cases in which Gemma 4 4B erred. In this case, the McNemar test produced $p = 0.0062$, indicating a significant advantage of SwinYNet at the 0.5 threshold.

The bootstrap analysis of the scores reinforces the probabilistic advantage of SwinYNet. For Gemma 4 2B, the delta (VLM minus SwinYNet) was -0.0518 in ROC-AUC, with a 95% confidence interval between

TABLE VII. Probabilistic performance metrics computed over the continuous `frb_probability` score, for the three systems. The metrics are defined in Sect. VI (for the Brier score and the ECE, lower values are better).

Model	ROC-AUC	Average Precision	Brier score	ECE
Gemma 4 2B	0.9482	0.9336	0.0655	0.1011
Gemma 4 4B	0.9309	0.9102	0.0878	0.0706
SwinYNet	1.0000	1.0000	0.0569	0.1096

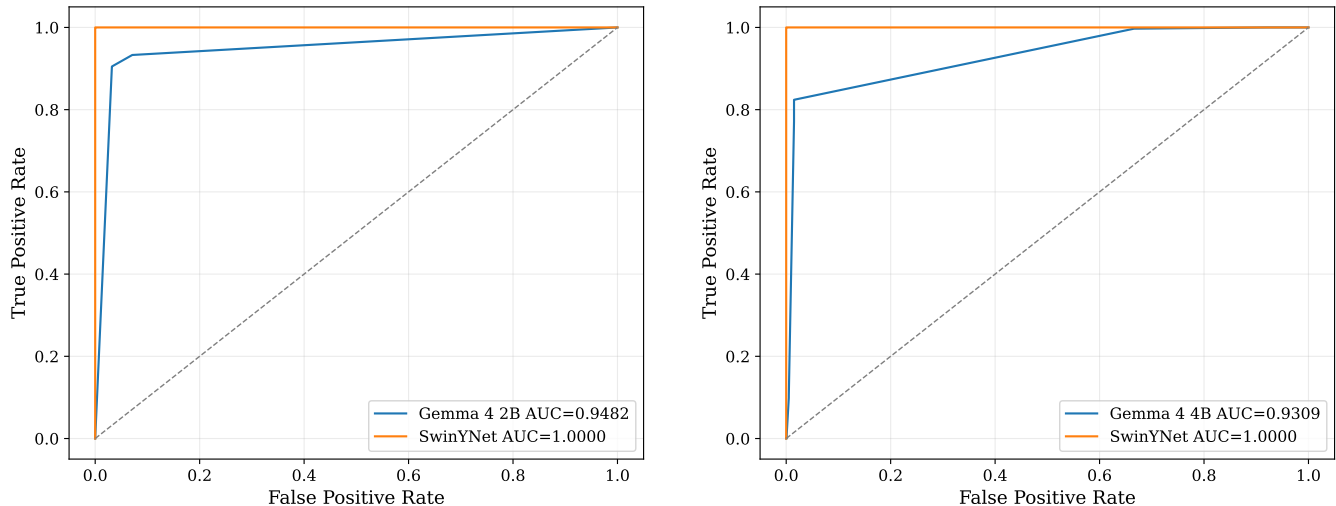


FIG. 3. ROC curves for the binary FRB versus NON_FRB task. Left: Gemma 4 2B; right: Gemma 4 4B. In each panel, the specialized detector SwinYNet attains a perfect ranking ($AUC = 1.0000$), whereas the staircase shape of the VLM curve reflects the small number of distinct `frb_probability` values.

-0.0616 and -0.0423 ; for Average Precision, the delta was -0.0664 , with an interval between -0.0805 and -0.0530 . For Gemma 4 4B, the deltas were even more negative: -0.0691 in ROC-AUC and -0.0898 in Average Precision.

These results support a balanced reading that is favorable to the thesis of the VLMs’ potential. At the default operating point, the discrete decisions of Gemma 4 2B show no statistically significant difference from those of a dedicated detector (McNemar $p = 0.3305$), although SwinYNet remains superior as a probabilistic classifier on this benchmark. That a generalist model, without training and without access to the FITS, performs at the level of a specialized detector at the default threshold, with no statistically significant difference, is, by itself, strong evidence of what the approach is capable of doing.

D. False positives by non-FRB type

The stratification of the false positives by source class is one of the most revealing results about what the generalist VLM actually learned. The NON_FRB class aggregates RFI and noise, but these two groups represent different difficulties for a search pipeline. Structured RFI

tends to produce more problematic false candidates than stochastic noise, because it can partially mimic coherent structures in the dynamic spectrum.

At the 0.5 threshold (Table IX), SwinYNet classified 125 of the 500 RFI samples as FRB, producing $FPR_{RFI} = 0.250$. Gemma 4 2B produced 32 false positives on RFI ($FPR_{RFI} = 0.064$), and Gemma 4 4B produced 15 ($FPR_{RFI} = 0.030$). On noise, the VLMs produced no false positives, while SwinYNet classified 17 of the 500 noise samples as FRB ($FPR_{NOISE} = 0.034$). Because the three systems were evaluated on the same samples, this gap can be tested directly. Restricting the McNemar test to the 500 RFI samples gives $p = 3.8 \times 10^{-21}$ for Gemma 4 2B versus SwinYNet (94 samples in which only the VLM is correct, against 1 in which only SwinYNet is correct) and $p = 1.8 \times 10^{-24}$ for Gemma 4 4B (112 against 2), so the better RFI rejection of the VLMs at this operating point is statistically significant.

This table shows that the VLM is not merely recognizing the shape of an FRB. It actively rejects structured RFI, which is precisely the most difficult type of contaminant. At the default threshold, Gemma 4 2B and 4B classified as FRB only 6.4% and 3.0% of the RFI samples, against 25% for SwinYNet, and no VLM produced a false positive on pure noise. For a model that was never trained on this task, distinguishing structured interference from a dispersed track is a concrete demonstration

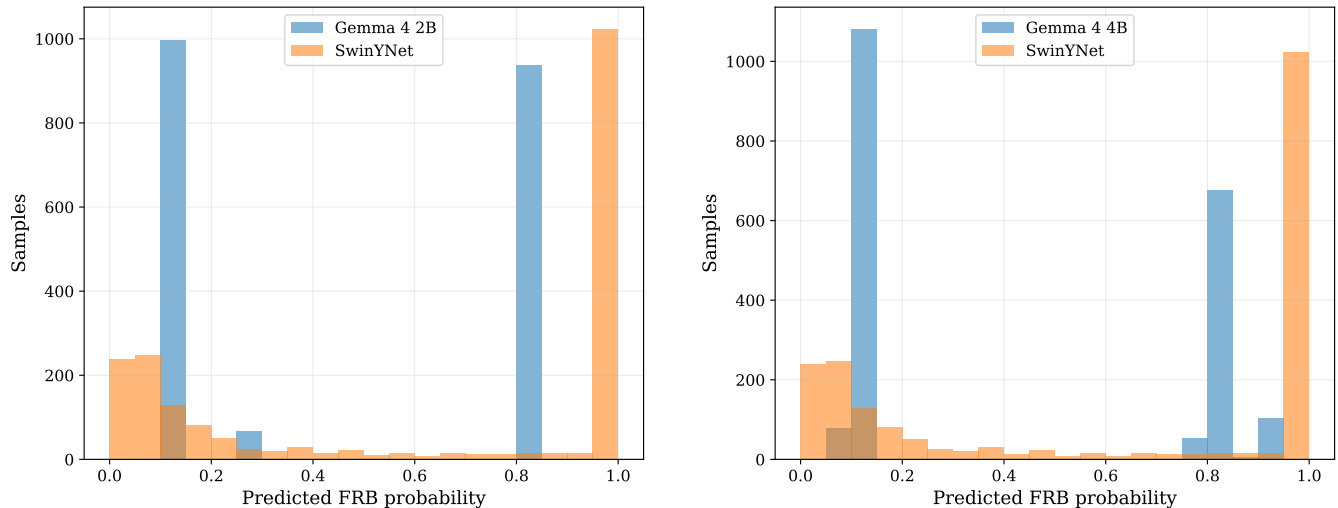


FIG. 4. Histograms of the predicted `frb_probability` for the binary task. Left: Gemma 4 2B; right: Gemma 4 4B. The VLM scores concentrate on a few discrete values, illustrating the strong quantization discussed in the text, whereas the specialized detector SwinYNet saturates near 0 and 1.

TABLE VIII. Paired comparison between each VLM and SwinYNet at the 0.5 threshold, over the same samples. The disagreements column counts the samples for which the two models assigned different labels, and the two following columns split them between the cases in which only the VLM was correct and those in which only SwinYNet was correct. The McNemar test reported in the last column is defined in Sect. VI.

Comparison	Disagreements	VLM right / SwinYNet wrong	SwinYNet right / VLM wrong	McNemar p
Gemma 4 2B vs SwinYNet	207	111	96	0.3305
Gemma 4 4B vs SwinYNet	307	129	178	0.0062

of potential, and it suggests that the approach could, in real streams with many false RFI candidates, help reduce the inspection load.

This conclusion must be limited to the current benchmark. The data are simulated, the RFI categories are controlled, and the decision threshold was not optimized for a real survey. Even so, the result shows that the VLM goes beyond replicating the decision of the specialized detector; it errs differently, and this difference may have practical value.

E. Computational cost and operational use

As detailed in Sect. VB, the mean inference time was 5.4 s per file for Gemma 4 2B and 7.8 s per file for Gemma 4 4B, measured on the workstation described there, in a sample-by-sample regime and without batching. Since each simulated file contains 2 s of observation, these times, which represent an upper bound in this unoptimized configuration, do not support a brute-force real-time search over a continuous data stream.

On the other hand, this cost is already perfectly acceptable for the triage of pre-selected candidates or for hybrid pipelines, and it tends to decrease substantially with batching, quantization, or even smaller models. It

is also the scenario in which the textual explainability of the VLM adds the most value, since, in addition to deciding, the model justifies the decision in natural language, something rare in specialized detectors.

F. Disagreements and cases exclusive to the VLM

The disagreement files show that there are cases in which only the VLM is correct and cases in which only SwinYNet is correct. This information is richer than the aggregate accuracy. For Gemma 4 2B, there were 111 samples in which the VLM was correct and SwinYNet erred, against 96 in which the opposite occurred. In addition, 31 samples were wrong for both models. For Gemma 4 4B, there were 129 correct answers exclusive to the VLM, 178 correct answers exclusive to SwinYNet, and 13 common errors. The fact that there are dozens of samples that only the VLM gets right indicates that the generalist model captures visual patterns that the specialized detector lets through.

To characterize these disagreements, each sample was cross-referenced with its source class and simulation parameters, and the pattern is clear and almost symmetric.

The VLM’s exclusive correct answers fall entirely on the negative class. For Gemma 4 2B, the 111

TABLE IX. False positives by `NON_FRB` source type at the 0.5 threshold. The false-positive columns count, for each model, how many `RFI` and `NOISE` samples were classified as `FRB`, out of the 500 of each type. The FPR is defined in Sect. VI, with lower values indicating better rejection of that contaminant.

Model	False positives on RFI	FPR RFI	False positives on NOISE	FPR NOISE
Gemma 4 2B	32/500	0.064	0/500	0.000
Gemma 4 4B	15/500	0.030	0/500	0.000
SwinYNet	125/500	0.250	17/500	0.034

samples in which the VLM is right and SwinYNet is wrong are 94 RFI and 17 noise, with no FRB, that is, cases in which the specialized detector produced a false positive and the VLM correctly rejected it. Among the RFI, the `wifi_multiband` type dominates (67 of 94), followed by `persistent_narrowband` (13), `impulsive_broadband` (6), `point_to_point_microwave` (4), and `satellite_like_inband` (4). The VLM’s exclusive gain therefore lies precisely in structured RFI, especially multiband interference, the contaminant hardest to distinguish from a transient.

The exclusive errors of VLMs, in turn, are almost only faint FRBs. For Gemma 4 2B, 95 of the 96 samples in which SwinYNet is right and the VLM is wrong are FRBs that the VLM missed (the 96th is an RFI). These FRBs are systematically of low intensity. The median flux density of the missed FRBs is 4.81, against 7.87 for the full FRB set (same internal units as Sect. IV D), and 67 of the 95 fall below the global 25th percentile (5.84); none exceeds 8.33, whereas the maximum of the set is 11.98. In the visual attributes reported by the model itself, these cases appear as having no visible structure and a random background texture. That is, the VLM perceived them as noise, consistent with FRBs of low visual intensity in the PNG.

Gemma 4 4B repeats the same profile even more markedly. Of the 129 exclusive correct answers, 112 are RFI (85 `wifi_multiband`) and 17 noise; and of the 178 exclusive errors, 176 are faint FRBs, with a median flux density of 5.37 and 104 of the 176 below the global 25th percentile (5.84).

This characterization turns the paired comparison into qualitative evidence of the VLM’s behavior. The generalist model does not err randomly relative to the dedicated detector, since it gains exactly where SwinYNet stumbles, rejecting structured RFI that the detector confuses with an FRB, and loses exactly on the faintest FRBs, near the detection limit. In real streams with many false RFI candidates, this complementary behavior has practical value, although the loss of faint FRBs calls for caution regarding the fraction of FRBs recovered.

G. Multiclass classification

In addition to the binary task, a multiclass formulation was tested with the three labels `FRB`, `RFI`, and `NOISE`. This experiment is not the main axis of the comparison

TABLE X. Per-class metrics for the multiclass task (`FRB/RFI/NOISE`), for both VLMs, on 1000 samples per class. Metrics and support are defined in Sect. VI.

Model	Class	Precision	Recall	F1-score	Support
Gemma 4 2B	<code>FRB</code>	1.0000	0.8700	0.9305	1000
	<code>RFI</code>	0.9889	0.5340	0.6935	1000
	<code>NOISE</code>	0.6289	1.0000	0.7722	1000
Gemma 4 4B	<code>FRB</code>	1.0000	0.9210	0.9589	1000
	<code>RFI</code>	0.9565	0.6600	0.7811	1000
	<code>NOISE</code>	0.7199	1.0000	0.8372	1000

with SwinYNet, but it illustrates the flexibility of the VLM in redefining the task through the prompt.

Both models were evaluated on the full simulated set of 3000 samples described in Sect. IV, with 1000 samples per class. This set is a superset of the binary benchmark, containing the same 1000 FRB samples together with all 1000 RFI examples (200 per subtype) and all 1000 NOISE examples, whereas the binary evaluation used 500 of each negative class. Gemma 4 4B reaches an overall accuracy of 86.0% (macro F1-score of 0.859) and Gemma 4 2B reaches 80.1% (macro F1-score of 0.799). The per-class metrics for both models are reported in Table X.

The error structure is shared by the two models and is informative in itself. The `FRB` class is recovered with perfect precision (1.0000). No RFI or NOISE sample is ever labeled FRB, so the reconfiguration to three classes introduces no false FRB. The `NOISE` class is recovered with perfect recall (1.0000). Every noise sample is identified as such. The whole difficulty concentrates in the `RFI` class, whose recall (0.6600 for Gemma 4 4B and 0.5340 for Gemma 4 2B) is limited by the faintest interference subtypes, which are systematically confused with `NOISE` rather than with `FRB`. Broken down by subtype, `persistent_narrowband` and `wifi_multiband` are recovered perfectly by both models, whereas the two faintest categories concentrate the loss. `point_to_point_microwave` (recall 0.075 for Gemma 4 2B and 0.260 for Gemma 4 4B) and `satellite_like_inband` (0.075 and 0.325, in the same order) account for 370 of the 466 and 283 of the 340 RFI-to-NOISE errors of the two models, with `impulsive_broadband` in an intermediate position (0.520 and 0.715). This mirrors the faint-FRB behavior of the binary task. An interference signal whose visual contrast approaches the noise floor of the rendered image is read

as noise, in line with the dependence on the visual representation discussed in Sect. VIH.

The mean inference time was 3.8 s per file for Gemma 4 2B and 4.3 s per file for Gemma 4 4B, below the binary-task figures reported in Sect. VB. This reduction follows directly from the design of the multiclass prompt. The instruction is deliberately compact and defines RFI as a residual class, anything that is neither a single dispersed sweep nor pure noise, instead of enumerating the interference morphologies present in the benchmark, which would encode dataset-specific priors into the classifier. Its structured output is correspondingly lighter, dropping the probability field and the per-feature diagnostic block requested in the binary task, so that fewer instruction and output tokens are processed per image. Consistently with the demonstrative role of this experiment, no per-class prompt tuning was pursued; the multiclass prompt is reproduced in full in Appendix B.

Even in this deliberately simple setting, the result is one of the clearest pieces of evidence of the potential pursued in this work. Without any retraining, and only by rewriting the prompt, the same model separates three classes and tells pure noise apart from structured RFI and from dispersed bursts. This reconfiguration of the task through natural language is something that a supervised detector does not offer without a new training cycle.

H. Threats to validity

Some limitations must be made explicit so that the results are interpreted correctly.

First, the benchmark is simulated. This ensures label control, balancing, and reproducibility, but it does not capture the full complexity of real observational data, including instrumental effects, RFI variability, calibration, masking, defective channels, and real signal-to-noise distributions. Therefore, validation on real data is a necessary step before any broad operational claim.

Second, the comparison between the VLM and SwinYNet is asymmetric. SwinYNet was developed as a specialized detector and operates on FITS, while the VLM receives only a PNG image. This asymmetry favors the specialized detector in terms of access to information and should be seen as part of the experimental design. Precisely for this reason, the performance of Gemma 4 2B, so close to SwinYNet at the default threshold, is notable, but it should not be described as proof of general superiority.

Third, the dataset is balanced. This choice is appropriate for an initial controlled comparison, but it does not represent the real prevalence of FRBs in astronomical searches. In real scenarios, even a small false-positive rate can generate many false candidates. For this reason, Precision-Recall curves, threshold analyses, and evaluations under rare priors must be discussed before operational use is proposed.

Fourth, the VLM depends on the visual representation. Colormap, normalization, resolution, contrast, and cropping can affect the decision. The result presented here holds for the image protocol described in Sect. IV. Future studies should test visualization ablations [65, 66] and compare the robustness to different ways of representing the same FITS. The same care applies to the design of the textual prompt, since the outputs of generalist VLMs can vary with changes in the structure of the instruction [43]. As discussed in Sect. VE, deterministic decoding removes only the stochastic variation, not this dependence on the prompt, so that the results hold for the fixed prompt reproduced in Appendix A.

Fifth, the probabilities produced by the VLMs in this run are quantized into few distinct values (three for Gemma 4 2B, nine for Gemma 4 4B). This makes the probabilistic and calibration metrics coarse and limits the ROC and Precision-Recall curves to few operating points. As indicated in Sect. VIB, obtaining a finer continuous score is the next methodological step to make this part of the evaluation conclusive.

Sixth, the evaluation is zero-shot with respect to this benchmark, in the sense that no labeled example from it is shown to the models, but the data used to pretrain generalist VLMs may include dynamic-spectrum figures of FRBs from the scientific literature. Some indirect prior exposure to the visual concept of a dispersed burst therefore cannot be excluded. This does not affect the paired comparison on these newly simulated images, but it should temper any reading of the results as evidence that the models had no previous contact with the domain.

Finally, the textual justifications of the VLM are useful for auditing, but they should not be automatically treated as correct physical explanations. A model can produce a plausible justification for a wrong decision. Thus, interpretability here should be understood as inspectability of the decision, not as a guarantee of physical causality.

VII. CONCLUSIONS

This work shows that generalist, small, and local VLMs, used only with a prompt and without any specific training, have a real potential for the analysis of FRB signals.

In the FRB versus NON_FRB task, Gemma 4 2B and 4B achieved an accuracy of 0.90–0.94 and a ROC-AUC of 0.93–0.95, with Gemma 4 2B showing no statistically significant difference from a specialized detector at the default threshold and rejecting RFI significantly more efficiently. Moreover, the same model proved capable of going beyond the binary decision and separating FRB, RFI, and NOISE only by changing the prompt.

SwinYNet remains the performance reference, with a perfect probabilistic ranking on this benchmark. It is to be seen as a ceiling of a dedicated detector, to which a

zero-shot generalist model comes surprisingly close.

The value of this work is not in declaring a winner, but in demonstrating that a generalist, inexpensive, and interpretable tool already recognizes FRB, RFI, and noise patterns with little domain information. This opens the way for applications in radio astronomy (triage, diagnosis, and the detection of signal types not anticipated in the training of specialized models), and motivates the next steps, such as a finer probabilistic score, DM estimation, and validation on real data. In addition, the adaptation techniques deliberately left out of this study — in-context (few-shot) learning, fine-tuning, retrieval-augmented generation (RAG), and agents or calls to external tools — can still be employed to further improve the results.

ACKNOWLEDGMENTS

The work of A.R.Q. is supported by FAPESQ-PB. A.R.Q. acknowledges support by CNPq under process number 310533/2022-8. K.E.L.F., R.A.B., T.S.S.D. thank the Paraíba State Research Support Foundation (FAPESQ) for financial support. The work of R.H.S.

and K.E.L.F. is supported by CNPq.

DATA AVAILABILITY

The code that generates, classifies, and evaluates the samples, together with the benchmark metadata (the label and image manifests), the per-sample predictions of the three systems, and the evaluation outputs, is openly available in the project repository at https://github.com/raiffhugo/frb_svlm. The simulated PSR-FITS files and the rendered images are too large to be hosted in the repository (about 60 GB); they can be regenerated exactly from the pinned configuration and global seed described in Sect. IV, and are also available from the corresponding author upon reasonable request.

The pipeline is implemented in Python and builds on open-source software: `simulateSearch` [44, 58], Hugging Face Transformers [60], PyTorch [67], NumPy [68], scikit-learn [69], Matplotlib [70], and Astropy [71].

Appendix A: Binary classification prompt

The full binary prompt supplied to the model in the FRB versus NON_FRB task is reproduced below, exactly as sent to the model.

```

You are an expert radio astronomer classifying dynamic-spectrum images from a transient-search pipeline.

Image meaning:
- x-axis: time
- y-axis: frequency
- intensity: signal power

Classify the image as exactly one of:
- FRB
- NON_FRB

Return ONLY valid JSON. No markdown, no comments, no extra keys.

Decision rules:

1. FRB candidates
Label as FRB only when the dominant signal is a SINGLE localized transient that is plausibly broadband and shows a frequency-dependent arrival-time trend, usually later arrival at lower frequency. The sweep may be curved, nearly linear, faint, or partially masked.

2. Low-S/N sensitivity
Do not treat faint coherent structure as pure noise. If there is any plausible faint diagonal/curved sweep, localized broadband brightening, partial dispersed track, or excess variance along a tilted band, use an intermediate probability instead of a very low one.

3. NON_FRB cases
Label as NON_FRB when the image is dominated by:
- pure random background with no coherent transient,
- persistent horizontal frequency bands,
- persistent vertical time bands,
- periodic stripes or grid-like structure,
- zero-DM broadband vertical impulse with no dispersion delay,
- saturation, clipping, blank regions, uniform panels, or normalization artifacts,
- two or more temporally separated broadband pulses or repeating patterns.

4. Probability calibration
frb_probability must be in [0,1].

```

Use the full range and avoid always reusing the same values.

Calibration guide:

- 0.95-0.99: textbook FRB, clear broadband dispersed sweep.
- 0.80-0.94: probable FRB with minor ambiguity.
- 0.60-0.79: plausible FRB but faint, partial, or noisy.
- 0.45-0.59: genuinely ambiguous.
- 0.30-0.44: weak possible structure, more likely NON_FRB.
- 0.18-0.29: likely noise or weak contamination.
- 0.05-0.17: clear RFI, persistent bands, artifacts, or strong NON_FRB evidence.
- 0.01-0.04: blank, saturated, clipped, or unambiguous artifact.

Label consistency:

- label = "FRB" only if frb_probability \geq 0.50
- label = "NON_FRB" only if frb_probability $<$ 0.50

confidence is how certain you are about the discrete label, not the FRB probability.

Output exactly this JSON schema:

```
{
  "label": "FRB|NON_FRB",
  "frb_probability": 0.0,
  "confidence": 0.0,
  "reason": "short explanation referencing the visual evidence",
  "features": {
    "visible_structure": true,
    "broadband": true,
    "localized_transient": true,
    "frequency_dependent_delay": true,
    "persistent_bands": false,
    "repeating_pattern": false,
    "uniform_or_constant_background": false,
    "saturated_or_clipped": false,
    "random_background_texture": false
  }
}
```

Feature definitions:

- visible_structure: any coherent visual structure is present.
- broadband: signal spans a substantial frequency range.
- localized_transient: signal is confined to a short time interval.
- frequency_dependent_delay: arrival time changes systematically with frequency.
- persistent_bands: horizontal or vertical bands persist across much of the panel.
- repeating_pattern: multiple pulses, stripes, grids, or periodic structures.
- uniform_or_constant_background: panel is nearly blank or constant.
- saturated_or_clipped: image has saturation, clipping, or rectangular masked regions.
- random_background_texture: dominated by stochastic noise with no coherent candidate.

The reason must be one short sentence.

Appendix B: Multiclass classification prompt

The prompt supplied to the model in the multiclass FRB/RFI/NOISE task is reproduced below, exactly as sent.

In contrast to the binary prompt, it defines RFI as a residual class rather than enumerating interference morphologies, and requests a lighter JSON output without the probability field or the per-feature block.

You are an expert in radio astronomy analyzing candidate images from a transient-search pipeline.

The image is a dynamic spectrum: the horizontal axis is time, the vertical axis is frequency, and pixel intensity is signal power.

Classify the image into exactly one of three classes: FRB, RFI, or NOISE.
Decide only from the visual content of the image.

Class definitions

=====

NOISE

The entire panel is featureless, stochastic background texture. There is no coherent structure anywhere: no lines, no stripes, no bands, no localized bright spots, no sweep, nothing but random fluctuations.

FRB

A single astrophysical burst: one localized, broadband transient whose arrival time changes systematically (monotonically) with frequency, tracing a single continuous sweep across the band. It appears only once, is confined in time, and neither repeats nor sits at a fixed frequency.

RFI

Anything else. Any image that is not pure NOISE and is not a single dispersed FRB sweep is RFI, i.e. any coherent, persistent, repeated, or artificial-looking structure of terrestrial or instrumental origin.

Decision procedure

=====

1. Is there a single broadband sweep that drifts monotonically in frequency with time? If yes, label FRB.
2. Otherwise, is the panel pure random texture with no coherent feature at all? If yes, label NOISE.
3. Otherwise, label RFI.

Rules

=====

- NOISE requires a complete absence of coherent structure. If you can see ANY non-random feature anywhere in the panel -- even faint, even sparse, even a single thin line, a streak, or a few repeated marks -- the image is NOT NOISE.
- Faint or sparse structure still counts as structure.
- An FRB drifts in frequency and appears once. Signals that stay at a fixed frequency, form horizontal or vertical bands, or repeat in time are RFI, not FRB.
- When unsure between RFI and NOISE, choose RFI. When a single drifting broadband sweep is unsure between FRB and RFI, prefer FRB.

Output

=====

Return ONLY a valid JSON object with this exact schema, and nothing else:

```
{
  "label": "FRB|RFI|NOISE",
  "confidence": 0.0,
  "reason": "one short sentence citing the visual evidence"
}
```

confidence is how certain you are about the chosen label.

Do not include markdown, code fences, comments, or any text outside the JSON object.

-
- [1] D. R. Lorimer, M. Bailes, M. A. McLaughlin, D. J. Narkevic, and F. Crawford, “A bright millisecond radio burst of extragalactic origin,” *Science*, vol. 318, no. 5851, pp. 777–780, 2007.
- [2] J. I. Katz, “Fast radio bursts—a brief review: Some questions, fewer answers,” *Modern Physics Letters A*, vol. 31, no. 14, p. 1630013, 2016.
- [3] E. Petroff, J. W. T. Hessels, and D. R. Lorimer, “Fast radio bursts,” *The Astronomy and Astrophysics Review*, vol. 27, no. 1, p. 4, 2019.
- [4] B. Zhang, “The physical mechanisms of fast radio bursts,” *Nature*, vol. 587, pp. 45–53, 2020.
- [5] B. Zhang, “The physics of fast radio bursts,” *Reviews of Modern Physics*, vol. 95, no. 3, p. 035005, 2023.
- [6] K. M. Rajwade and J. van Leeuwen, “A needle in a cosmic haystack: A review of FRB search techniques,” *Universe*, vol. 10, no. 4, p. 158, 2024.
- [7] W.-Q. Ma and Z.-F. Gao, “The properties of fast radio bursts: A short review,” *Astronomische Nachrichten*, vol. 346, no. 7, p. e20250024, 2025.
- [8] E. Petroff *et al.*, “A real-time fast radio burst: polarization detection and multiwavelength follow-up,” *Mon. Not. Roy. Astron. Soc.*, vol. 447, no. 1, pp. 246–255, 2015.
- [9] J. M. Cordes and S. Chatterjee, “Fast Radio Bursts: An Extragalactic Enigma,” *Ann. Rev. Astron. Astrophys.*, vol. 57, pp. 417–465, 2019.
- [10] K. Bandura, G. E. Addison, M. Amiri, J. R. Bond, D. Campbell-Wilson, L. Connor, J.-F. Cliche, G. Davis, M. Deng, N. Denman, *et al.*, “Canadian hydrogen intensity mapping experiment (CHIME) pathfinder,” in *Ground-based and Airborne Telescopes V*, vol. 9145, p. 914522, SPIE, 2014.
- [11] S. Johnston, M. Bailes, N. Bartel, C. Baugh, M. Bietenholz, C. Blake, R. Braun, J. Brown, S. Chatterjee, J. Darling, *et al.*, “Science with the Australian square kilometre array pathfinder,” *Publications of the Astronomical Society of Australia*, vol. 24, no. 4, pp. 174–188, 2007.
- [12] R. Nan, D. Li, C. Jin, Q. Wang, L. Zhu, W. Zhu, H. Zhang, Y. Yue, and L. Qian, “The five-hundred-meter aperture spherical radio telescope (FAST) project,” *International Journal of Modern Physics D*, vol. 20, no. 06, pp. 989–1024, 2011.
- [13] F. Camilo, P. Scholz, M. Serylak, S. Buchner, M. Merrifield, V. Kaspi, R. Archibald, M. Bailes, A. Jameson, W. v. Straten, *et al.*, “Revival of the magnetar PSR J1622–4950: Observations with MeerKAT, Parkes, XMM-Newton, Swift, Chandra, and NuSTAR,” *The Astrophysical Journal*, vol. 856, no. 2, p. 180, 2018.
- [14] T. Lemos, R. S. Gonçalves, J. C. Carvalho, and J. S. Alcaniz, “Cosmological model-independent constraints on the baryon fraction in the IGM from fast radio bursts and supernovae data,” *Eur. Phys. J. C*, vol. 83, no. 2, p. 138, 2023.
- [15] J. A. S. Fortunato, W. S. Hipólito-Ricardi, and M. V.

- dos Santos, “Cosmography from well-localized fast radio bursts,” *Mon. Not. Roy. Astron. Soc.*, vol. 526, no. 2, pp. 1773–1782, 2023.
- [16] T. Lemos, R. Gonçalves, J. Carvalho, and J. Alcaniz, “Cosmological model-independent limits on photon mass from FRB and SNe data,” *JCAP*, vol. 11, p. 019, 2025.
- [17] L. L. Sales, K. E. L. de Farias, A. R. Queiroz, J. R. L. Santos, R. A. Batista, A. R. M. Oliveira, L. F. Santana, C. A. Wuensche, T. Villela, and J. Vieira, “Cosmographic constraints from late-time probes including fast radio bursts,” 7 2025.
- [18] L. L. Sales, K. E. L. de Farias, A. R. Queiroz, R. A. Batista, B. W. Ribeiro, and R. H. Santos, “Constraints on the baryon density from fast radio bursts using a non-parametric reconstruction of the Hubble parameter,” 5 2026.
- [19] J. R. L. Santos, G. Domènech, and A. R. Queiroz, “Probing Primordial Black Holes with upcoming Radio Telescopes: a case study for LOFAR2.0, FAST Core Array and BINGO,” 4 2026.
- [20] B. W. N. Ribeiro, L. L. Sales, K. E. L. de Farias, R. H. Santos, R. A. Batista, and A. R. Queiroz, “Constraints on Dark Energy and Modified Gravity Models from Fast Radio Bursts and Late-Time Geometric Probes,” 6 2026.
- [21] J. H. Cao, P. Wang, D. Li, Q. H. Pan, K. Mao, C. H. Niu, Y. K. Zhang, Q. Y. Qu, W. J. Lu, and J. S. Zhang, “BASSET: Bandpass-adaptive single-pulse search toolkit—optimized subband pulse search strategies for faint narrowband fast radio bursts,” *The Astrophysical Journal Supplement Series*, vol. 280, no. 1, p. 12, 2025.
- [22] X. Yang, G. Hobbs, S.-B. Zhang, A. Zic, L. Toomey, Y. Li, J.-S. Wang, S. Dai, and X.-F. Wu, “Searching for short-time-scale radio anomalies using non-linear dimensionality reduction techniques,” *Monthly Notices of the Royal Astronomical Society*, vol. 537, pp. 991–1000, February 2025.
- [23] X. Yang, S.-B. Zhang, J.-S. Wang, and X.-F. Wu, “Classifying frb spectrograms using nonlinear dimensionality reduction techniques,” *Monthly Notices of the Royal Astronomical Society*, vol. 522, pp. 4342–4351, July 2023.
- [24] S. M. Ransom, *New search techniques for binary pulsars*. PhD thesis, Harvard University, Cambridge, MA, 2001. ADS Bibcode: 2001PhDT.....123R.
- [25] S. M. Ransom, “PRESTO: Pulsar exploration and search TOolkit.” Astrophysics Source Code Library, record ascl:1107.017, 2011. <https://ascl.net/1107.017>.
- [26] B. R. Barsdell, M. Bailes, D. G. Barnes, C. J. Fluke, A. Jameson, and I. G. Bebbington, “Accelerating incoherent dedispersion,” *Monthly Notices of the Royal Astronomical Society*, vol. 422, pp. 379–392, May 2012.
- [27] D. R. Lorimer and M. Kramer, *Handbook of pulsar astronomy*, vol. 4. Cambridge university press, 2005.
- [28] S. Belmonte Díaz *et al.*, “Enhancing fast radio transient detection with mask r-cnn image segmentation,” *RAS Techniques and Instruments*, vol. 5, no. 1, p. rzag006, 2026.
- [29] X. Guo, H. Wang, Y. Xiao, H. Chen, Y. Ke, C. Miao, P. Wang, D. Li, C. Jin, L. He, *et al.*, “Accelerating the fast radio burst search: Data set and methods,” *The Astrophysical Journal Supplement Series*, vol. 280, no. 1, p. 34, 2025.
- [30] A. Dosovitskiy, L. Beyer, A. Kolesnikov, D. Weissenborn, X. Zhai, T. Unterthiner, M. Dehghani, M. Minderer, G. Heigold, S. Gelly, J. Uszkoreit, and N. Houlsby, “An image is worth 16x16 words: Transformers for image recognition at scale,” in *International Conference on Learning Representations (ICLR)*, 2021.
- [31] Y. Chen, S. Ni, C. Li, J. Fang, D. Zhou, H. Chen, Y. Feng, P. Wang, C. Jin, H. Wang, *et al.*, “SwinYNet: A transformer-based multitask model for accurate and efficient fast radio burst searches,” *The Astrophysical Journal Supplement Series*, vol. 283, no. 2, p. 45, 2026.
- [32] S. Yin, C. Fu, S. Zhao, K. Li, X. Sun, T. Xu, and E. Chen, “A survey on multimodal large language models,” *National Science Review*, vol. 11, p. nwae403, 12 2024.
- [33] B. He, F. Zhao, Y. Wang, P. Chen, X. Wang, D. Ma, H. Xu, and H. Li, “AstroSight: Galaxy morphology classification with multimodal large language models,” *Publications of the Astronomical Society of the Pacific*, vol. 138, no. 4, p. 044508, 2026.
- [34] D. Tanoglidis, C. Y. Tan, K. Overdeck, and A. Drlica-Wagner, “Do vision-language models see dwarf galaxies the way we do?,” *arXiv preprint arXiv:2606.07779*, 2026. Accepted at the Conference on Physics and AI (PAI 2026).
- [35] S. Zaman, M. J. Smith, P. Khetarpal, R. Chakrabarty, M. Ginolfi, M. Huertas-Company, M. Jabłońska, S. Kruk, M. L. Lain, S. J. R. Méndez, *et al.*, “AstroLLaVA: towards the unification of astronomical data and natural language,” *arXiv preprint arXiv:2504.08583*, 2025. Accepted at the SCI-FM workshop at ICLR 2025.
- [36] I. Kamai, M. Huertas-Company, M. J. Smith, and H. B. Perets, “Talking with the latents — how to convert your LLM into an astronomer,” *arXiv preprint arXiv:2602.09670*, 2026.
- [37] F. Stoppa, T. Bulmus, S. Bloemen, S. J. Smartt, P. J. Groot, P. Vreeswijk, and K. W. Smith, “Textual interpretation of transient image classifications from large language models,” *Nature Astronomy*, vol. 9, no. 12, pp. 1869–1878, 2025.
- [38] Gemini Team, R. Anil, S. Borgeaud, J.-B. Alayrac, J. Yu, R. Soricut, J. Schalkwyk, A. M. Dai, A. Hauth, K. Milan, *et al.*, “Gemini: a family of highly capable multimodal models,” *arXiv preprint arXiv:2312.11805*, 2023.
- [39] Gemma Team, “Gemma 4: Frontier Multimodal Intelligence on Device.” <https://deepmind.google/models/gemma/gemma-4/>, 2026. Released April 2026. Open weights under Apache 2.0. Google DeepMind.
- [40] F. Zhao, Y. Li, Y. Wang, H. Li, M. Chen, P. Chen, N. Sun, C. Wang, and J. Liu, “Pulsar candidate classification with multimodal large language models,” in *NeurIPS 2024 Workshop on Foundation Models for Science: Progress, Opportunities, and Challenges*, 2024.
- [41] F. Zhao, Y. Li, Z. Liu, P. Chen, C. Wang, J. Liu, H. Li, and Y. Wang, “Unveiling the power of multimodal large language models for radio astronomical image understanding and question answering,” *Machine Learning: Science and Technology*, vol. 6, no. 4, p. 045005, 2025.
- [42] S. Riggi, T. Ceconello, A. Pilzer, S. Palazzo, N. Gupta, A. Hopkins, C. Triglio, and G. Umana, “radio-llava: Advancing vision-language models for radio astronomical source analysis,” *Publications of the Astronomical Society of Australia*, vol. 42, p. e121, 2025.
- [43] M. Drozdova, E. Lastufka, V. Kinakh, T. Holotyak, D. Schaerer, and S. Voloshynovskiy, “Radio astronomy in the era of vision-language models: Prompt sensitivity and adaptation,” *arXiv preprint arXiv:2509.02615*, 2025.

- Presented at the Machine Learning and the Physical Sciences Workshop, NeurIPS 2025.
- [44] R. Luo, G. Hobbs, S. Y. Yong, A. Zic, L. Toomey, S. Dai, A. Dunning, D. Li, T. Marshman, C. Wang, P. Wang, S. Wang, and S. Zhang, “Simulating high-time resolution radio-telescope observations,” *Monthly Notices of the Royal Astronomical Society*, vol. 513, no. 4, pp. 5881–5891, 2022.
- [45] C. D. Bochenek, V. Ravi, K. V. Belov, G. Hallinan, J. Kocz, S. R. Kulkarni, and D. L. McKenna, “A fast radio burst associated with a galactic magnetar,” *Nature*, vol. 587, pp. 59–62, 2020.
- [46] J.-P. Macquart, J. Prochaska, M. McQuinn, K. Bannister, S. Bhandari, C. Day, A. Deller, R. Ekers, C. James, L. Marnoch, *et al.*, “A census of baryons in the universe from localized fast radio bursts,” *Nature*, vol. 581, no. 7809, pp. 391–395, 2020.
- [47] J. Yao, R. Manchester, and N. Wang, “A new electron-density model for estimation of pulsar and frb distances,” *The Astrophysical Journal*, vol. 835, no. 1, p. 29, 2017.
- [48] J. M. Cordes and T. J. W. Lazio, “NE2001. i. a new model for the galactic distribution of free electrons and its fluctuations,” *arXiv preprint astro-ph/0207156*, 2002.
- [49] Y.-K. Zhang, D. Li, Y. Feng, C.-W. Tsai, P. Wang, C.-H. Niu, H.-X. Chen, and Y.-H. Zhu, “DRAFTS: A deep-learning-based radio fast transient search pipeline,” *The Astrophysical Journal Supplement Series*, vol. 276, no. 1, p. 20, 2025.
- [50] H. Liu, C. Li, Q. Wu, and Y. J. Lee, “Visual instruction tuning,” in *Advances in Neural Information Processing Systems* (A. Oh, T. Naumann, A. Globerson, K. Saenko, M. Hardt, and S. Levine, eds.), vol. 36, pp. 34892–34916, Curran Associates, Inc., 2023.
- [51] W. Ren, H. Guo, W. Zuo, and X. Zhang, “A systematic evaluation of vision-language models for observational astronomical reasoning tasks,” *arXiv preprint arXiv:2604.24589*, 2026.
- [52] C. Chen, J. S. Xiao, S. D. Liu, F. P. Paolino, L. Handley, T. J. d. Laz, R. Nilsson, A. Zou, M. Graham, and A. Mahabal, “AstroAlertBench: Evaluating the accuracy, reasoning, and honesty of multimodal LLMs in astronomical classification,” *arXiv preprint arXiv:2605.05573*, 2026.
- [53] J. Shi, X. Tang, Y. Huang, Y. Li, X. Kong, Y. Zhang, and C. Yue, “AstroMMBench: A benchmark for evaluating multimodal large language models capabilities in astronomy,” *arXiv preprint arXiv:2510.00063*, 2025.
- [54] A. Radford, J. W. Kim, C. Hallacy, A. Ramesh, G. Goh, S. Agarwal, G. Sastry, A. Askell, P. Mishkin, J. Clark, G. Krueger, and I. Sutskever, “Learning transferable visual models from natural language supervision,” in *Proceedings of the 38th International Conference on Machine Learning (ICML)*, vol. 139, pp. 8748–8763, PMLR, 2021.
- [55] Z. Liu, Y. Lin, Y. Cao, H. Hu, Y. Wei, Z. Zhang, S. Lin, and B. Guo, “Swin transformer: Hierarchical vision transformer using shifted windows,” in *Proceedings of the IEEE/CVF International Conference on Computer Vision (ICCV)*, pp. 10012–10022, 2021.
- [56] L. Parker, F. Lanusse, J. Shen, O. Liu, T. Hehir, L. Sarra, L. Meyer, M. Bowles, S. Wagner-Carena, H. Qu, *et al.*, “AION-1: Omnimodal foundation model for astronomical sciences,” *Advances in Neural Information Processing Systems*, vol. 38, pp. 95386–95428, 2026.
- [57] Gemma Team, T. Mesnard, C. Hardin, R. Dadashi, S. Bhupatiraju, S. Pathak, *et al.*, “Gemma: Open models based on Gemini research and technology,” *arXiv preprint arXiv:2403.08295*, 2024.
- [58] G. Hobbs, R. Luo, and L. Toomey, “simulateSearch: High-time resolution data sets simulations for radio telescopes.” Astrophysics Source Code Library, record ascl:2205.025, 2022. <https://ascl.net/2205.025>.
- [59] A. W. Hotan, W. van Straten, and R. Manchester, “PSRCHIVE and PSRFITS: an open approach to radio pulsar data storage and analysis,” *Publications of the Astronomical Society of Australia*, vol. 21, no. 3, pp. 302–309, 2004.
- [60] T. Wolf, L. Debut, V. Sanh, J. Chaumond, C. Delangue, A. Moi, P. Cistac, T. Rault, R. Louf, M. Funtowicz, J. Davison, S. Shleifer, P. von Platen, C. Ma, Y. Jernite, J. Plu, C. Xu, T. Le Scao, S. Gugger, M. Drame, Q. Lhoest, and A. M. Rush, “Transformers: State-of-the-art natural language processing,” in *Proceedings of the 2020 Conference on Empirical Methods in Natural Language Processing: System Demonstrations*, pp. 38–45, Association for Computational Linguistics, 2020.
- [61] G. W. Brier, “Verification of forecasts expressed in terms of probability,” *Monthly Weather Review*, vol. 78, no. 1, pp. 1–3, 1950.
- [62] C. Guo, G. Pleiss, Y. Sun, and K. Q. Weinberger, “On calibration of modern neural networks,” in *International conference on machine learning*, pp. 1321–1330, PMLR, 2017.
- [63] Q. McNemar, “Note on the sampling error of the difference between correlated proportions or percentages,” *Psychometrika*, vol. 12, no. 2, pp. 153–157, 1947.
- [64] B. Efron, “Bootstrap Methods: Another Look at the Jackknife,” *The Annals of Statistics*, vol. 7, no. 1, pp. 1–26, 1979.
- [65] R. Meyers, M. Lu, C. W. De Puiseau, and T. Meisen, “Ablation studies in artificial neural networks,” *arXiv preprint arXiv:1901.08644*, 2019.
- [66] S. Sheikholeslami, “Ablation programming for machine learning,” Master’s thesis, KTH Royal Institute of Technology, Stockholm, Sweden, 2019. <https://urn.kb.se/resolve?urn=urn:nbn:se:kth:diva-258413>.
- [67] A. Paszke, S. Gross, F. Massa, A. Lerer, J. Bradbury, G. Chanan, T. Killeen, Z. Lin, N. Gimelshein, L. Antiga, A. Desmaison, A. Köpf, E. Yang, Z. DeVito, M. Raison, A. Tejani, S. Chilamkurthy, B. Steiner, L. Fang, J. Bai, and S. Chintala, “Pytorch: An imperative style, high-performance deep learning library,” in *Advances in Neural Information Processing Systems*, vol. 32, 2019.
- [68] C. R. Harris, K. J. Millman, S. J. van der Walt, R. Gommers, P. Virtanen, D. Cournapeau, E. Wieser, J. Taylor, S. Berg, N. J. Smith, R. Kern, M. Picus, S. Hoyer, M. H. van Kerkwijk, M. Brett, A. Haldane, J. F. del Río, M. Wiebe, P. Peterson, P. Gérard-Marchant, K. Sheppard, T. Reddy, W. Weckesser, H. Abbasi, C. Gohlke, and T. E. Oliphant, “Array programming with NumPy,” *Nature*, vol. 585, no. 7825, pp. 357–362, 2020.
- [69] F. Pedregosa, G. Varoquaux, A. Gramfort, V. Michel, B. Thirion, O. Grisel, M. Blondel, P. Prettenhofer, R. Weiss, V. Dubourg, J. Vanderplas, A. Passos, D. Cournapeau, M. Brucher, M. Perrot, and É. Duchesnay, “Scikit-learn: Machine learning in Python,” *Journal of Machine Learning Research*, vol. 12, pp. 2825–2830, 2011.
- [70] J. D. Hunter, “Matplotlib: A 2D graphics environment,” *Computing in Science & Engineering*, vol. 9, no. 3, pp. 90–95, 2007.

- [71] Astropy Collaboration, A. M. Price-Whelan, P. L. Lim, N. Earl, N. Starkman, L. Bradley, D. L. Shupe, *et al.*, “The Astropy project: Sustaining and growing a community-oriented open-source project and the latest major release (v5.0) of the core package,” *The Astrophysical Journal*, vol. 935, no. 2, p. 167, 2022.